Bachelor thesis

Operating procedures of a demonstration experiment on H2 permeation from solar thermal receivers into silicone oil

Submitted by

Thomas Grünendahl

Matriculation number

756198

Degree Program

Mechanical Engineering

Hochschule Esslingen, Faculty of Mechanical and Systems Engineering

Supervisors

Prof. Dr. Ing. Walter Czarnetzki

Dr. Lukas Heller

Aichwald, October

2024

Abstract

This study investigated the operational methodology for hydrogen removal from solar thermal collector tubes. The process comprises three stages: hydrogen transport from the absorber tubes' vacuum insulation into the heat transfer fluid (HTF), transfer into the headspace gas of the expansion vessel, and venting into the atmosphere. For effective hydrogen removal, these stages must proceed at comparable rates.

Operational challenges, such as blockages in the system's piping and exceeding pressure limits, necessitated system modifications. As a result, this work focuses primarily on determining the mass flow rate of recirculated HTF using time-of-flight measurements.

Despite uncertainties introduced by noninvasive sensor installation and limited data logger resolution, the analysis confirmed that complete fluid recirculation is achievable within 34 minutes, allowing for multiple cycles daily without exceeding system pressure limits. Adjustments to the operating procedure further enabled continuous recirculation, enhancing overall system efficiency.

Table of contents

List of figures

List of tables

1 Introduction

The climate crisis poses a severe threat to the future sustainability of human civilization. The continued reliance on fossil fuel combustion is causing global temperatures to rise, destabilizing climate systems and leading to increasingly frequent and severe weather extremes. To address these challenges, 196 countries ratified the Paris Agreement in 2015, committing to limit global warming to a maximum of 2.0°C above pre-industrial levels, while striving for a target below 1.5°C (UNFCCC, 2016)This goal was reaffirmed during the 2023 UN Climate Change Conference (COP 28) in Dubai (UNFCCC, 2023).

However, despite these efforts, global greenhouse gas emissions reached an unprecedented 57.4 gigatons of CO2 equivalent in 2022, with fossil fuel combustion and industrial activities contributing about two-thirds of this total (UNEP, 2023). To mitigate these impacts, the transition to renewable energy sources is essential. Solar energy alone holds tremendous potential, receiving approximately 120 petawatts of sunlight daily, enough to meet global energy demands for over two decades (Jibran Khan, 2015).

Renewable energy (RE) currently accounts for around 30% of the global energy mix, with projections suggesting an increase to 50% by 2030 (IEA, 2023). Wind and solar energy, particularly photovoltaics (PV), are expected to drive most of this growth due to their cost advantages over other energy sources (IEA, 2023). Nevertheless, PV and wind energy face challenges related to their variability and limited storage options, which hinder their capacity to ensure continuous power supply.

To overcome these limitations, solar thermal power plants, or Concentrating Solar Power (CSP) systems, offer a promising solution. These systems integrate energy generation with storage, enabling electricity production even during non-sunny periods. When coupled with Thermal Energy Storage (TES), CSP systems can provide reliable, on-demand power, complementing PV's daytime production (IEA, 2019). While CSP technology is becoming more cost-effective, it remains less economical than PV, posing a challenge for broader adoption (REEEM, 2017).

A critical component of CSP plants is the Heat Transfer Fluid (HTF), traditionally an organic mixture. However, the decomposition of these fluids over time results in hydrogen generation, leading to significant thermal efficiency losses. Addressing this issue involves either complex venting processes or expensive receiver tube replacements. A potential alternative is the use of silicon-based HTFs like HELISOL XLP, which offer enhanced chemical stability and reduced hydrogen production.

This research examines the feasibility of using HELISOL XLP to mitigate hydrogen accumulation in CSP systems, focusing on its application in the KONTAS test bench

at the Plataforma Solar de Almería. Modifications to the venting process and subsequent evaluations of hydrogen concentration will guide further system improvements.

2 Solar power: state of the art

There are currently two commercially available technologies for solar power generation: photovoltaics (PV) and concentrating solar power (CSP). PV utilizes the photoelectric effect to convert sunlight directly into electricity. To do this PV only needs the diffuse components of the sunlight, therefore it is usable in areas having both low as well as high direct normal irradiation (DNI). CSP on the other hand concentrates the light of the sun and therefore is in contrast only operable with high DNI (H.L. Zhang et. al., 2012). This heat is then used to power a turbine that converts the heat into electricity.

2.1 Irradiation

The Irradiation, the energy from the sun that constantly reaches the atmosphere of our planet, is about 1360 W/m². This value is reduced due to sunlight scattered by molecules and aerosols in the atmosphere, weather conditions, changing seasons, and the sun's elevation throughout the day. Some of these losses are still available in the form of diffuse solar radiation, which means all non-direct sunlight.

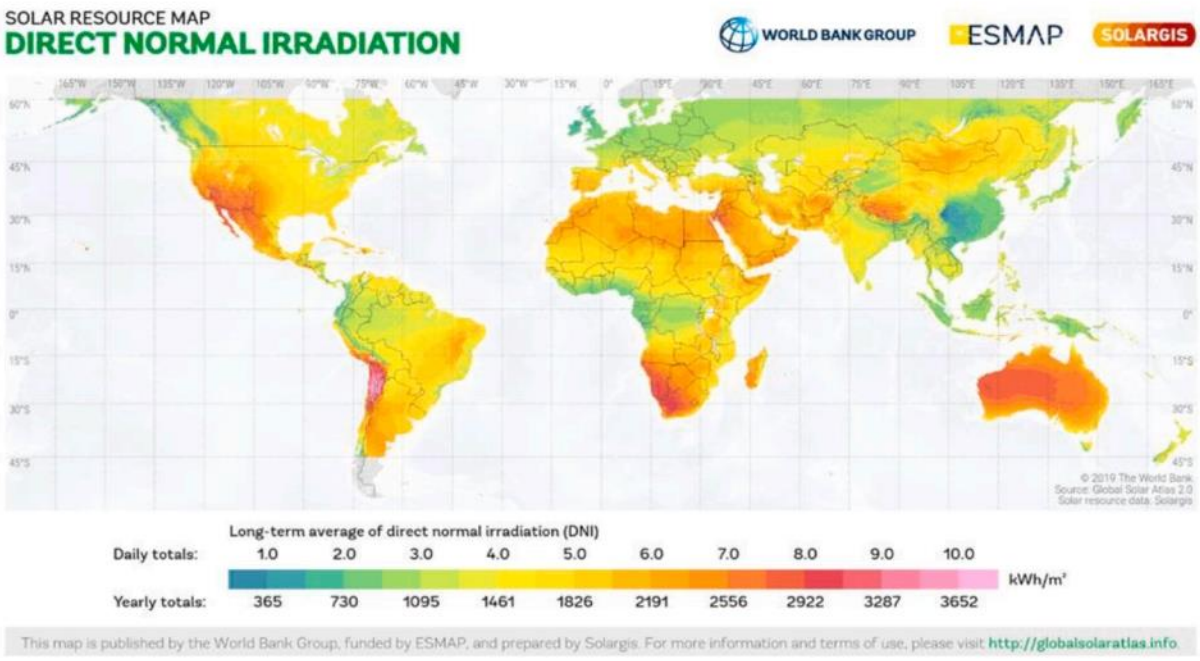

Figure 1 Direct normal irradiation worldwide (global solar atlas, 2024)

In consequence the DNI changes drastically for different regions of the world, like in Figure 1 shown. The best suitable regions are the South-West of the USA, Northern Chile, Southern Africa, Australia, Middle East, Northern Africa and the Mediterranean region. In general, it can be stated that desert regions display the highest DNI values.

The map shows the vast potential for solar power generation and that location is one of the major deciding factors in the planning of a new CSP plant. To express this factor in numbers, CSP developers determined areas with annual DNI above 1900 kWh/m²

as suitable for the operation of CSP. Below that threshold value solar electric technologies that work with both direct and diffuse irradiance, like photovoltaics, are superior (IEA, Technology Roadmap Concentrating Solar Power, 2010).

2.2 Concentrating solar power

Through the usage of mirrors CSP systems concentrate sunlight onto a receiver. The at this point accumulated heat is then transported by a heat transfer fluid (HTF) to either supply a power block (PB) that converts the thermal energy in a conventional power cycle first with a turbine into mechanical energy and subsequently into electricity in a generator. Alternatively, the thermal energy can be stored in a thermal energy storage (TES) for later use. The four most developed CSP technologies are linear Fresnel reflector, parabolic trough collector (PTC), solar tower and parabolic dish as seen in Figure 2.

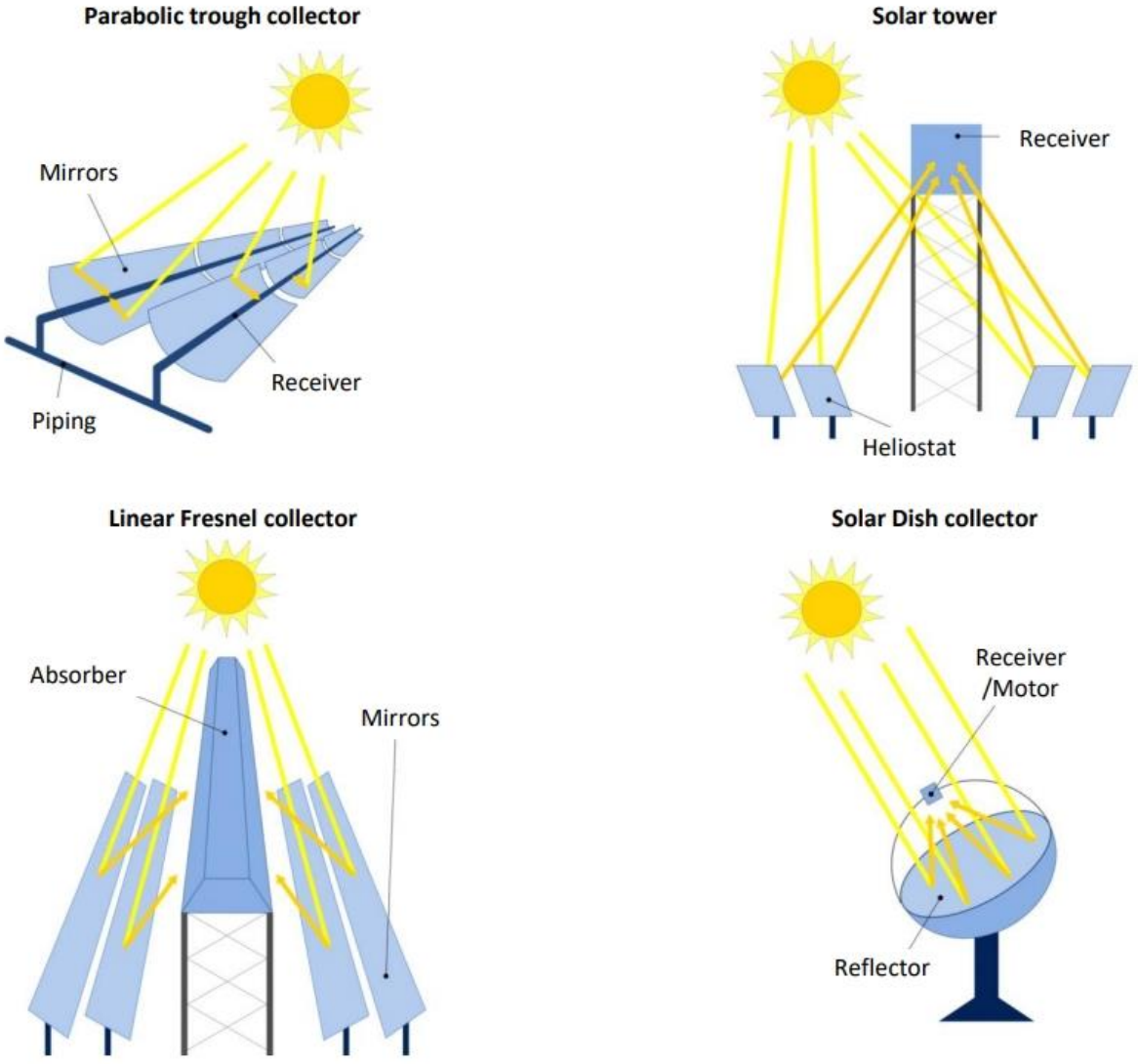

Figure 2 Concentrating solar power technologies (Wehner, 2022) based on (Pitz-Paal, 2020)

Whereas parabolic dish and solar tower belong to the point concentrating technologies, which means that the sunlight is concentrated in only one point, PTC and linear Fresnel reflector are line concentrators, which means that the heat is accumulated in a line-shaped receiver. While the advantage of point-focusing systems is that they reach higher concentration factors and operate with higher temperatures, line-focusing systems are usually simpler and more economic to implement (Wehner, 2022).

2.3 Parabolic trough collector power plants

PTC power plants consist of three parts: the solar field with several rows of parabolic trough collectors, the power block and the thermal energy storage.

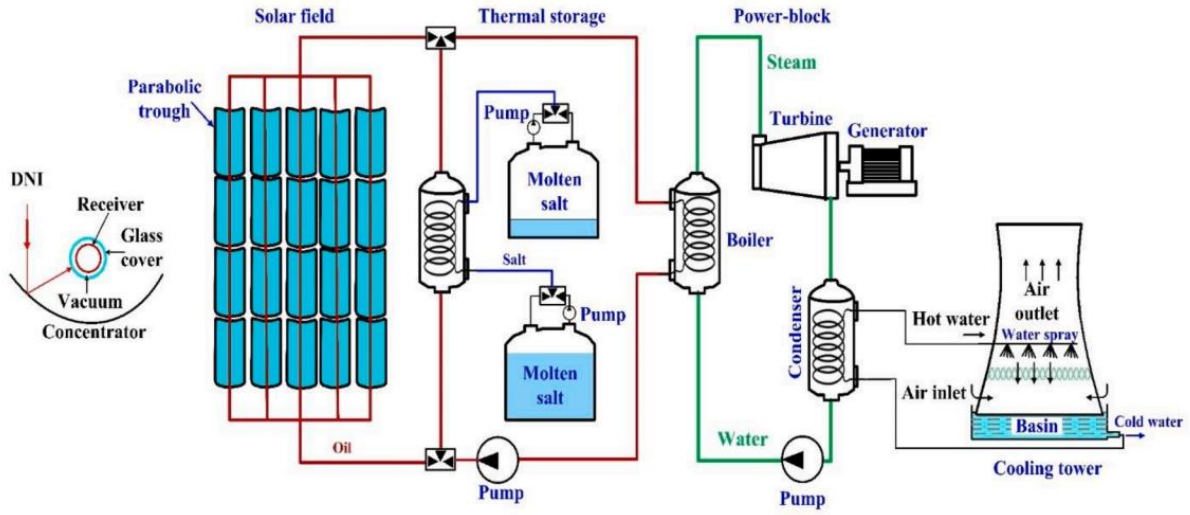

Figure 3 PTC power plant schematic (Abdul Hai Alami et. al., 2023)

2.3.1 Solar field

The solar field is composed of an organized framework, beginning with the smallest unit: a single PTC module. Each module typically measures 12 meters in length and 6 meters in width, covering an approximate area of 70 m². These modules are grouped into solar collector assemblies (SCAs), consisting of 4 to 12 modules. Each SCA is equipped with a single electric or hydraulic drive, enabling the assembly to move as a unified unit to focus sunlight onto the receiver tube.

To maximize energy collection, SCAs are further organized into loops, which consist of four to six SCAs arranged in two parallel rows. HTF flows continuously through the entire loop, absorbing solar energy and increasing in temperature from approximately 300 °C to 400 °C during its journey.

Multiple loops combine to form a solar subfield, and several subfields are interconnected to create the complete solar field, see Figure 4. This modular design enables scalability and efficient operation of the solar field. The heat is then transported by the HTF either directly to the heat exchanger of the PB or to the one of the TES system.

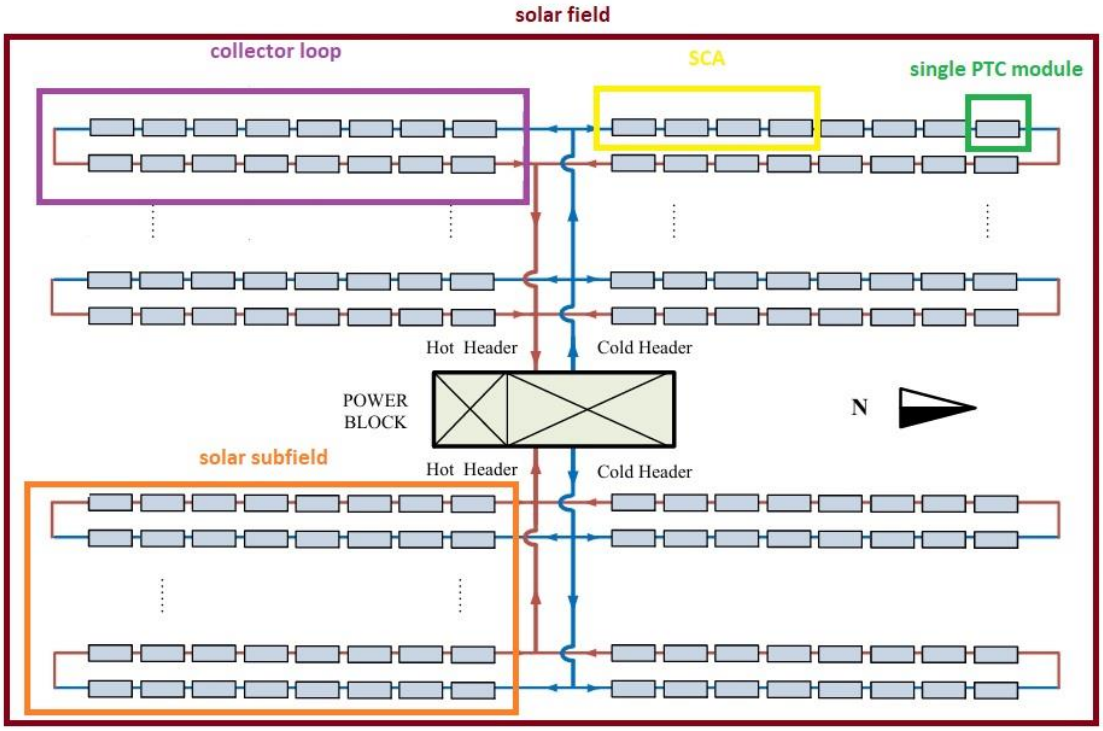

Figure 4 Structure of the solar field of a PTC power plant; figure adapted from (Padilla, 2011)

2.3.2 Thermal energy storage

The biggest advantage of CSP compared to PV is the possibility to store the heat in TES. In this way it is possible to bridge the night and cloudy days (absence of sun) and in consequence produce electricity 24 hours a day and 7 days a week in world regions with sufficient DNI. Furthermore, TES is a green technology and the commercially used molten salt is around 33 times cheaper per stored kWh than electric batteries (Wehner, 2022).

There are three types of TES: sensible, latent and thermochemical heat storage.

Sensible heat storage systems are the simplest way to store heat. The thermal energy is stored by changing the temperature of a storage medium. The relationship between temperature and energy is proportional, which means that the more energy is put in a material, the higher its temperature (ARANER, 2024).

In contrast latent TES systems utilize the phase change of a material, which means transitioning from gas to liquid or from liquid to a solid. During that process, heat is released or absorbed, which is then used to either store energy during the absorption or get energy out of the storage during release. Compared to sensible heat storage systems the energy storage potential of latent TES systems is much higher. Regarding water for example, it can provide approximately 80 times more energy during melting than rising its temperature from 1 to 2 degrees (ARANER, 2024).

Thermochemical storage systems generate heat by combining or separating two substances in a reversible chemical reaction. Depending on the exact used material, one of the processes is exothermic which means release of heat the other endothermic which means absorption. The biggest advantage of this storage type is that it is possible to store the energy long-term, over several months or even years (ARANER, 2024).

The most widely used TES method in CSP plants is the dual-tank indirect molten salt technology. This system operates as a sensible heat storage method, ensuring that the molten salt remains in its liquid phase, avoiding both solidification and gasification. The system includes a heat exchanger, which transfers thermal energy from the HTF to the molten salt, as well as one or more hot and cold tanks for storing the molten salt at high and low temperatures, respectively (Abdul Hai Alami et. al., 2023).

2.3.3 Power block

Within the Power block the collected thermal energy is converted to electric energy. This happens in 2 steps, a thermodynamical and an electromechanical conversion. First the heat is inside a turbine converted to mechanical energy, the so-called Rankine cycle. This mechanical energy in turn is then transformed into electricity by a generator.

2.4 Parabolic trough collector

Making up 75% of the totally globally installed CSP power, parabolic trough collectors (PTC) are the most mature technology to use thermal energy in sunlight. PTC systems use, as the name implies, parabolic shaped reflectors out of polished silver or aluminum to concentrate the sunlight onto their focal line. In that focal line their heat collecting element (HCE) is positioned.

This HCE consists of the receiver tube and the surrounding glass pipe. In between the receiver tube and the glass pipe is a vacuum to insulate the hot receiver tube from the comparable cold ambient and minimize heat losses at this position. Through the receiver tube is a constant flow of HTF, which absorbs the receiver tube’s heat and transports it either to the PB of the plant to generate electricity or to the TES for later use. In Figure 5 the principle structure of a typical PTC is shown.

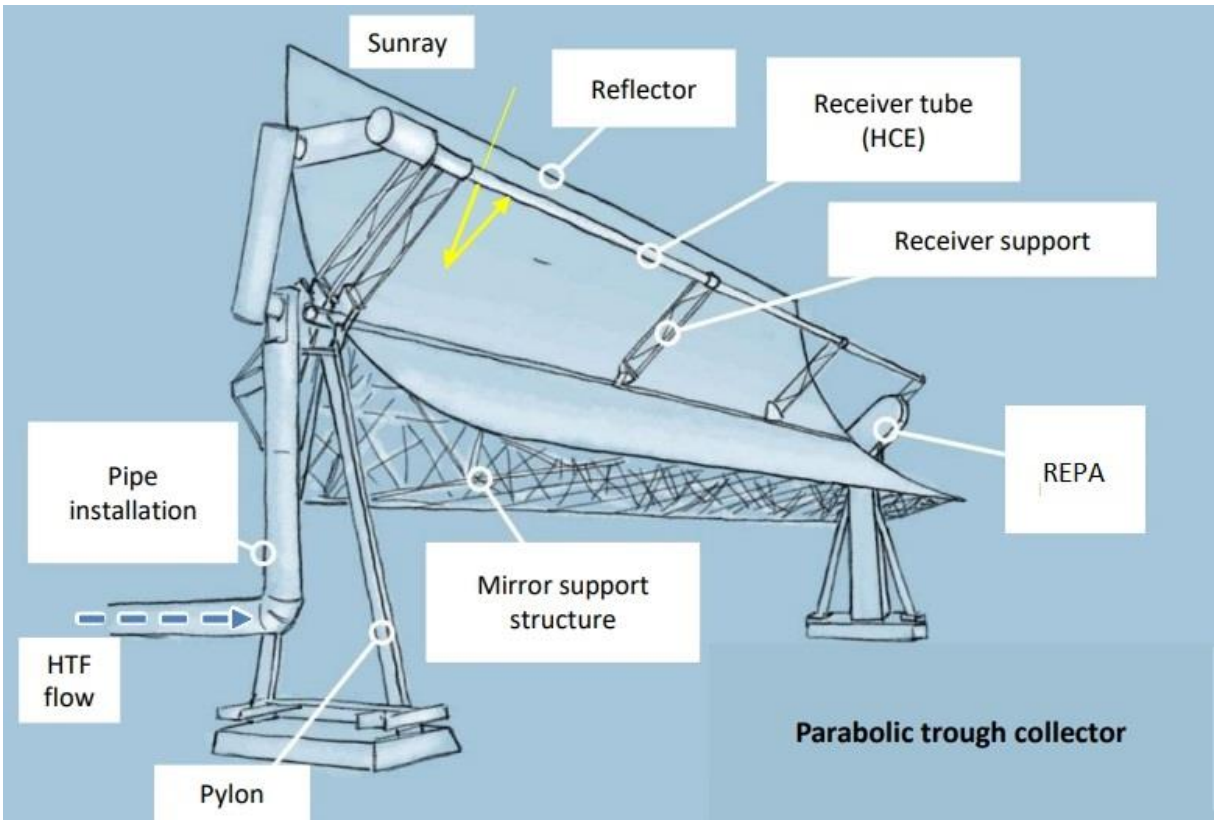

Figure 5 Composition of a parabolic trough collector (modified following (Wehner, 2022)).

Typically, PTCs are aligned in north-south axis, which enables them to track the sun from east to west and maximize the collected thermal energy and consequently their energy output. To enable this axial movement, the reflectors and absorber tubes of PTCs are rotatable.

The problem is that the focal line and the rotation axis are not aligned. This leads to high forces on the structural parts of the collector. Additionally, the length of the absorber tube varies its length over the day. It expands during daytime due to thermal expansion while heating up to the working temperature of 400 °C and contracts during cooling down to ambient temperature at night.

Both these jobs are fulfilled by the Rotation and Expansion Performing Assemblies, for short REPA. REPAs are designed to withstand these constant temperature induced expansions and contractions while simultaneously rotating to follow the sun for 25 to 30 years.

2.5 Heat collecting element

The heat collecting element (HCE) is a critical component in parabolic trough systems, designed to convert solar radiation into thermal energy. It consists of a metallic absorber tube, typically made of stainless steel, surrounded by a concentric glass envelope. This configuration enhances thermal efficiency by reducing heat losses and

protecting the system from environmental factors. To address the differing thermal expansion rates of glass and steel, bellows are incorporated at the tube ends, allowing for compensation during temperature fluctuations. The detailed structure of an HCE is illustrated in Figure 6.

The annular space between the absorber tube and the glass is hermetically sealed to maintain a vacuum, which is essential for minimizing conductive and convective heat losses. This design prevents the ingress of air and moisture, preserving the integrity of the system over time (Li et. al., 2012).

Two main factors can compromise the performance of HCEs: air ingress and HTF degradation. Air ingress, often caused by poor installation or maintenance, increases pressure within the annular space, reducing insulation effectiveness and thermal efficiency (H. Price et al., 2006). HTF degradation under prolonged high temperatures generates byproducts, notably hydrogen, which can permeate the steel absorber tube and reduce vacuum quality.

To mitigate these issues, non-evaporable getters are placed inside the annular space to capture permeated hydrogen, sustaining the vacuum over the HCE's operational lifetime. However, elevated hydrogen concentrations in the HTF can saturate the getters prematurely, reducing their effectiveness and potentially leading to substantial efficiency losses for the CSP system (C. Jung et al, 2019).

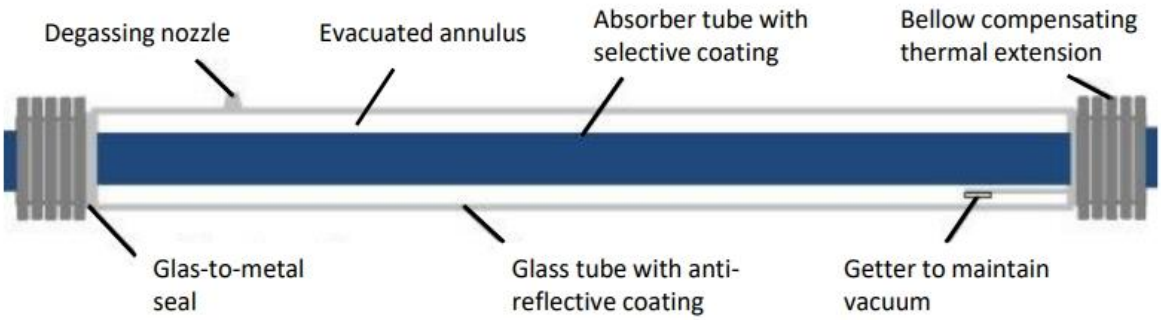

Figure 6 Heat collecting element with all parts in detail (Wehner, 2022)

2.6 Heat transfer fluid

State-of-the-art organic HTFs, such as the widely used eutectic mixtures of diphenyl oxide (DPO) and biphenyl (BP) under the trade names Dowtherm A, Therminol VP-1, and Diphyl, have been the standard for PTC power plants. These HTFs are valued for their physical and chemical properties, including favorable vapor pressure, density, heat capacity, and low corrosion tendency. However, they exhibit several critical limitations.

2.6.1 Limitations of organic HTFs

The operating temperature range of DPO/BP is limited to 12 °C to 400 °C. This restricts the thermal efficiency of PTC power plants, as efficiency improves with higher operational temperatures. Falling below the freezing point of 12 °C requires elaborate freeze protection systems, including auxiliary heating and trace heating, which add costs and energy consumption while increasing fire risks. The 6% volumetric contraction upon freezing also imposes mechanical stress on equipment (Dow Chemical Company, 1997).

DPO/BP also undergoes thermal degradation, producing hazardous byproducts like benzene and phenol. Benzene is a known carcinogen, creating health and environmental risks. Decomposition generates molecular hydrogen, which permeates the absorber tubes, degrading the vacuum insulation and increasing thermal losses.

The need for frequent maintenance during winter due to freezing risks reduces plant availability and increases operational costs. The environmental and occupational health risks associated with degraded DPO/BP raise concerns for long-term use.

2.6.2 Advantages of Silicone-Based HTFs

In contrast to organic, silicone-based HTFs, such as HELISOL XLP, offer several advancements that address these issues.

HELISOL XLP operates at temperatures up to 425 °C, significantly higher than DPO/BP, enhancing gross power block efficiency by 1.5% (C. Jung et al., 2014) and reducing dumping losses. The lower minimum operating temperature of -45 °C eliminates the need for extensive freeze protection measures, reducing costs and risks (Wacker Chemie AG, 2024).

Silicone-based HTFs degrade more slowly, generating less hydrogen and other decomposition products even at higher temperatures. This reduces the risk of hydrogen permeation into HCEs, prolonging their lifespan and maintaining thermal efficiency. Studies by DLR (Christoph Hilgert et al., 2019) have shown that silicone-based HTFs exhibit superior thermal stability, forming significantly less hydrogen at 425 °C compared to DPO/BP at 400 °C, see Figure 7.

Lower thermal inertia allows for faster heating and cooling, improving the responsiveness of the solar field. Reduced degradation rates and lower maintenance requirements translate into higher system reliability and lower long-term operational costs.

Silicone-based HTFs have lower environmental and health risks due to their stability and reduced hazardous byproduct generation. The absence of freezing issues simplifies winter operations and minimizes downtime.

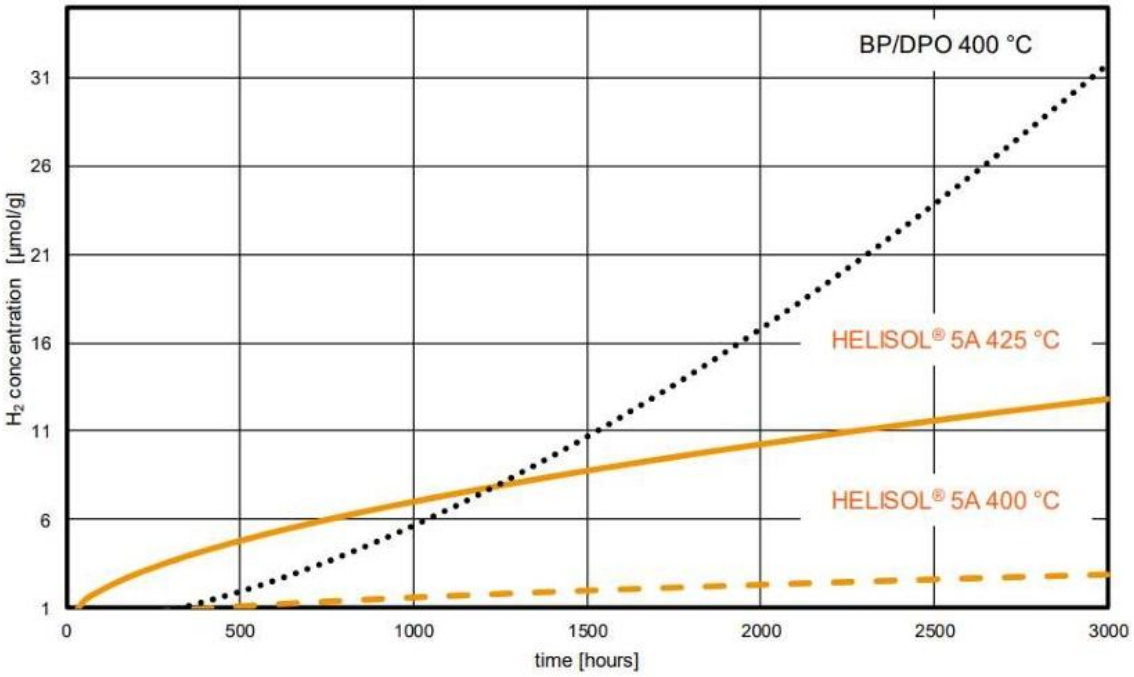

Figure 7 Hydrogen generation of Si-HTF (here HELISOL) and organic HTF (here DPO/BP) in comparison over lifetime (Wacker Chemie AG, 2020)

Although a complete replacement of HTFs in existing plants is uncommon due to high costs, the switch from DPO/BP to silicone-based alternatives like HXLP presents a significant opportunity for new plants and selective retrofitting.

2.7 Hydrogen permeation into heat collecting elements

Parabolic trough power plants have a long-standing performance issue relating to the build-up of trace quantities of hydrogen gas in the receiver tubes. Hydrogen is a by-product of the very slow breakdown of the heat transfer fluid. Accumulation of hydrogen in the receivers causes a loss in the thermal efficiency of the receivers and an overall decrease in the power plant annual electricity output. Since a typical plant contains 50,000 receivers, addressing this issue by individual receiver is not practical.

The National Renewable Energy Laboratory (NREL) conceived and developed a method to remove or purge hydrogen from the power plant receivers by removing hydrogen from a single location within the plant. Hydrogen gas is purged from the heat transfer fluid that resides in the power plant expansion tanks. Modeling shows that quantitative removal of hydrogen from the expansion tanks will reverse build-up of hydrogen in the receiver tubes and restore the power plant to its full performance and annual energy output (Glatzmaier, 2019).

3 Experimental setup

In this chapter the executive research institute, the project with all explicit goals for the experiment and the characteristics of the test site with all additional necessary modifications and preparations are described. Further it is explained what exactly is carried out during the project and which purpose it serves.

3.1 DLR

The experiments conducted in this thesis were carried out under the German Aerospace Center (DLR). It is Germany's largest research and development institution and was established to implement the national aerospace program and now conducts cutting-edge research in aeronautics, space, energy, transport, digitalization, and security.

One field is solar research, led by the DLR Institute of Solar Research, Germany's largest hub for Concentrated Solar Power (CSP) technologies. With over 30 years of expertise, the institute, formally established in 2011, employs more than 100 experts and is globally recognized for CSP research. Its operations span locations in Jülich, Stuttgart, Cologne, and Almería, Spain. The Almería site is hosted at CIEMAT's Plataforma Solar de Almería (PSA), a world-renowned test center for concentrating solar technologies.

3.2 Research project SiCo

The research project Si-Co: High Performance Parabolic Trough Collector and Innovative Silicone Fluid for CSP Plants is aimed at advancing the efficiency and reliability of CSP plants by introducing a novel HTF. The primary objective is to demonstrate the effectiveness of the new silicone-based HTF, HELISOL XLP, and to evaluate its potential as a replacement for the current state-of-the-art organic HTF, DPO/BP, in existing PTC power plants. This exchange promises to improve operational stability and thermal efficiency while addressing limitations associated with the current HTF.

One of the key aspects of the project involves testing the back-permeation of hydrogen from hydrogen-contaminated heat collection elements (HCEs). This process is crucial for enabling their thermal regeneration and ensuring long-term operational integrity within the CSP system. By addressing this challenge, the project aims to improve the overall performance and lifespan of key CSP components when utilizing HELISOL XLP as a replacement for traditional HTFs.

3.3 KONTAS test bench

KONTAS (KONzentrator Teststand Almeria Spanien) is a single module of a parabolic trough collector mounted on a rotatable platform (see Figure 8). Attached to it is the heating and cooling unit (HCU), responsible for cooling, heating and pumping. KONTAS was originally built to test different collector designs.

Figure 8 KONTAS test bench with its rotatable platform

3.3.1 Function of the HCU

The HCU system plays a vital role in maintaining the thermal regulation of the research facility's setup by providing reliable heating, cooling, and fluid circulation. The heating functionality of the HCU compensates for thermal transients during periods of insufficient solar energy, such as nighttime, cloudy days, or winter months when sunlight is weak even under clear skies. This capability is essential for achieving project goals that require a specific number of operating hours, as it enables continuous operation without dependence on sunlight. By utilizing the HCU's heating function, the overall time needed to reach project objectives is significantly reduced.

The cooling functionality of the HCU ensures temperatures remain stable and prevents overheating when the solar collector generates more heat than required. It also enables experiments that require rapid cooling, though this functionality was not utilized in the current study.

In addition to heating and cooling, the HCU is responsible for pumping fluid through the piping network to the solar collector, replicating the flow conditions typically observed in commercial power plants. By integrating these capabilities, the HCU

ensures operational flexibility, enhances reliability, and supports the research facility's diverse experimental needs.

3.3.2 Azimuth and elevation angle

It is possible to change the orientation of KONTAS in two different ways: with the elevation and azimuth the angle. Changing the elevation angle means rotating about the tracking axis. This means the collector is facing the sun directly all day, which means following it from east to west. This is achieved by the REPA system, which adjusts the elevation angle every 30-40sec for a perfect alignment. In Figure 9 it can be seen how a collector that is north-south aligned follows the position of the sun over the day through rotating around its tracking axis.

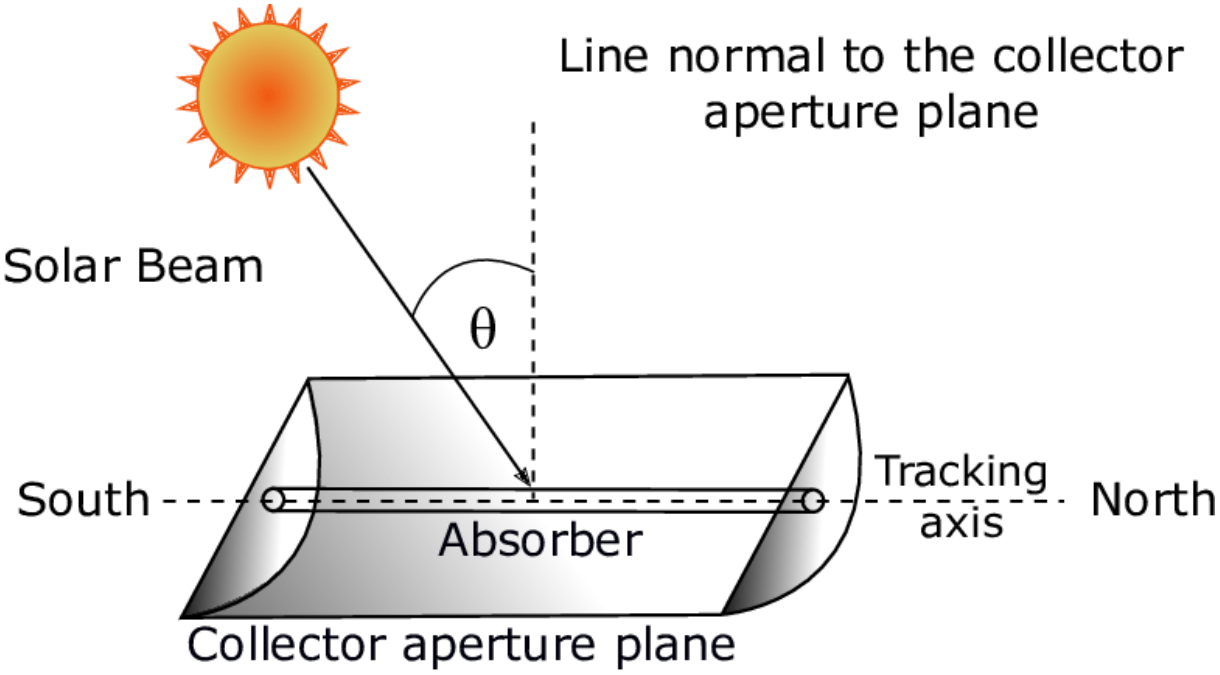

Figure 9 PTC tracking axis (Chethan R. Reddy et al., 2018)

While the possibility to adjust the elevation angle is common in commercial PTC power plants, it is a special feature of the KONTAS test bench that it is completely rotatable and due to this able to change its azimuth angle. The preferred alignment in commercial power plants is north-south because in this way the collectors are able to face the rising sun in the east in the morning and follow it until it sets in the west in the evening. With the rotatable platform it is also possible to switch to an east-west alignment or anything in between. This special ability enables KONTAS to simulate every day of the year with its unique sun angle.

Due to damage to one of the collector module's REPA systems, the elevation drive was not operational for the duration of this study. Hence, all thermal energy was derived from the electric heaters. The experiments to investigate the hydrogen removal from HCEs are not affected by the heating method used. To enable hydrogen back

permeation from the HCEs into the HTF, only the temperature of the HTF is relevant, not how it is heated.

3.4 Preparations

Several preparations and adjustments needed to be done at the KONTAS test bench before the experiments investigating hydrogen back-permeation could be carried out. The in chapter 3.4.1, 3.4.2 and 3.4.4 described works were executed before this thesis, but are necessary to understand the adaptions at KONTAS.

3.4.1 Installation of hydrogen-contaminated heat collecting elements

The original plan involved utilizing used heat collecting elements (HCEs) from a commercial plant that are already saturated with hydrogen. However, such HCEs were unavailable, necessitating a change in approach. As an alternative, used HCEs stored at the PSA were selected and deliberately contaminated with hydrogen. This contamination was carried out at the DLR laboratory in Cologne. The HCEs were loaded with hydrogen until the getters were fully saturated, and the hydrogen pressure within the annulus reached 1 1 mbar at 400 °C absorber tube temperature.

Following hydrogen loading, the performance of the HCEs was verified using CIEMAT´s HEATREC test bench, where measurements were taken both before and after the hydrogen loading procedure. These tests were conducted at 100 °C, 200 °C, 300 °C and 400 °C.

The results demonstrated a significant increase in heat loss at 400 °C, with values rising from an initial range of 210 W/m - 230 W/m to 796 W/m - 867 W/m after hydrogen loading - effectively quadrupling the heat loss. The variance in heat loss between the three HCEs tested was less than 10%, confirming similar loss behavior across the elements (Feulbach, 2024).

3.4.2 Doting of HELISOL XLP with DPO/BP

The KONTAS facility was originally built and run with the silicon oil Syltherm 800 as HTF. The first step to simulating an HTF changeover involved draining the Syltherm 800 from the system and refilling it with approximately 700 liters of HELISOL XLP. However, UV spectroscopy revealed that a significant residue of 8.8% (+/- 0.1%) Syltherm 800 remained in the system. This high residual value is likely due to the relatively large internal volume of heat exchangers, pumps, heaters, and other components, which are difficult to fully drain in a small-scale system. Despite the presence of these residues, the similarity between Syltherm 800 and HXLP, both being silicon-based fluids, ensures that this contamination does not pose any operational issues for the planned simulations, as the two fluids exhibit comparable thermal properties.

In contrast, the changeover of HTFs in commercial plants, where diphenyl oxide/biphenyl (DPO/BP) is commonly used, poses greater operational risks due to the formation of hydrogen. To simulate the effects of such contamination, DPO/BP from a

commercial CSP plant was introduced into the KONTAS HTF cycle. Previous testing of HTF changeover in the PROMETEO facility at the PSA, which utilized a larger system consisting of two rows of eight parabolic trough modules each and associated components such as expansion tanks and pumps, demonstrated a contamination of 1-2 wt.% DPO/BP after changeover. This level of contamination, while challenging to reduce further without significant expense, is considered realistic for commercial-scale plants.

To replicate these conditions, approximately 17 kg of DPO/BP was added to the KONTAS HTF cycle. Subsequent UV spectroscopy confirmed a contamination level of 1.9wt.% (+/- 0.1%), which aligns with previous observations and provides a realistic scenario for further experimental simulation of HTF changeover effects in commercial operations (Feulbach, 2024).

3.4.3 Optimal position for venting

Experiments carried out by Glatzmaier determined the optimal position for venting in PTC power plants to remove H_2 out of the system. The analysis (Glatzmaier, 2019) was based on a full-plant steady-state model of the Nevada Solar One PTC power plant, located in Boulder City, Nevada. The results from this model provided insights into the most effective venting strategies for parabolic trough systems.

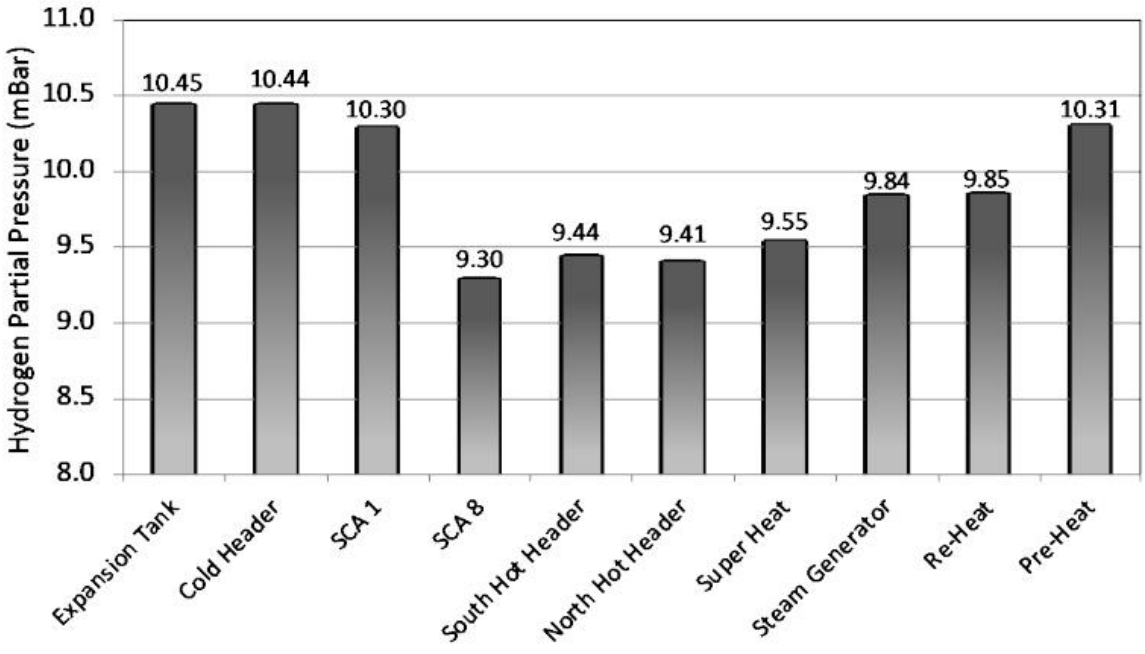

Figure 10 Hydrogen partial pressure in different PTC power plant components (Glatzmaier, 2019)

The optimal position for venting is determined by locating the point of highest hydrogen partial pressure, which was identified through experimental analysis (see Figure 10).

These experiments provided the necessary data to pinpoint the best venting location within the system.

In addition to identifying the area with the highest hydrogen partial pressure, ease of accessibility and minimal disruption to plant operations are key factors. Within the loop and the solar field, the HTF is actively flowing, so venting in these areas could disturb the fluid flow and affect system performance. Therefore, placing the venting point inside the expansion tank, where no flow occurs, would prevent interference with the HTF circulation and ensure smooth operation while facilitating maintenance access.

3.4.4 Sampling, recirculation and venting system

One of the key advantages of using a silicon-based HTF as the HTF in CSP plants is its negligible hydrogen formation, even at operating temperatures of 400°C. This characteristic helps prevent future hydrogen-induced problems in HCEs in newly built systems which use Si-HTFs.

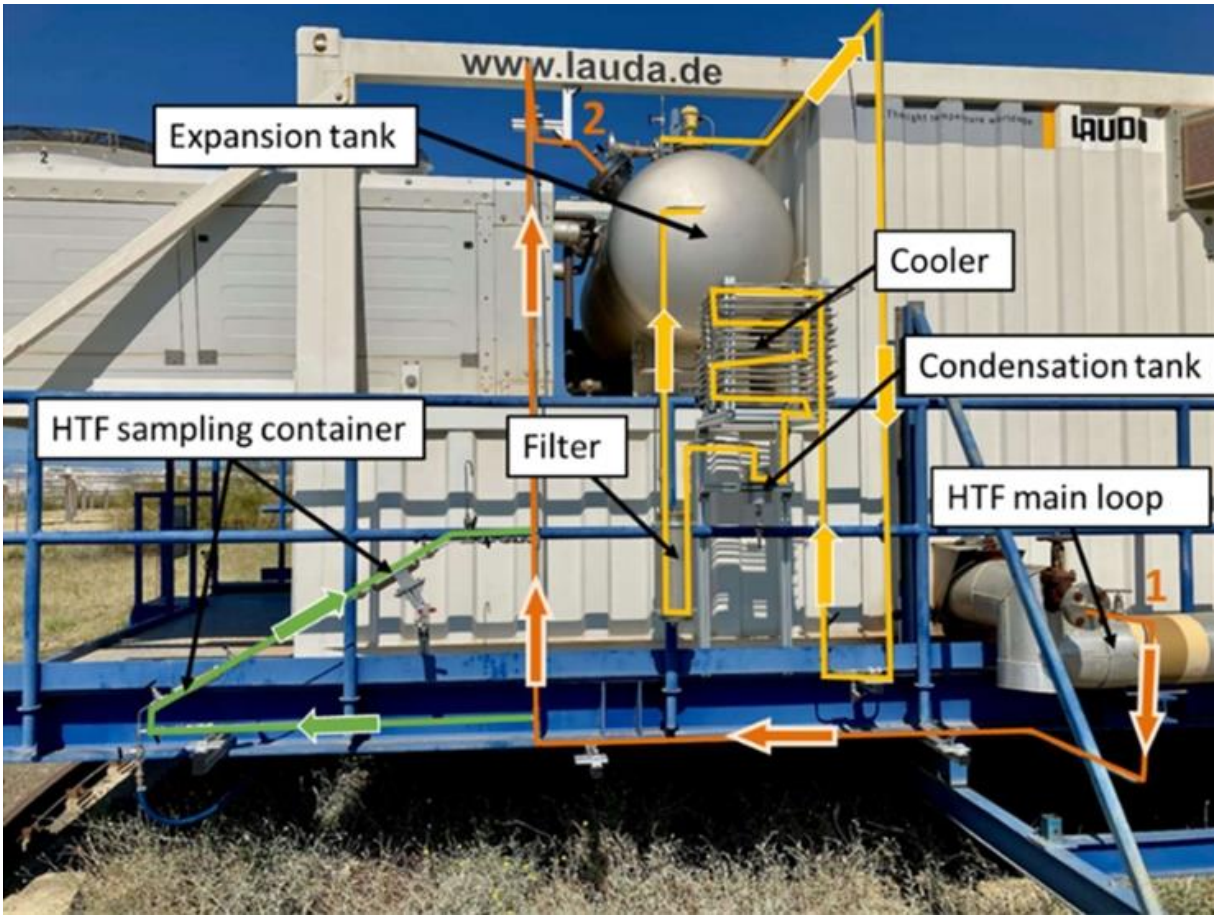

Figure 11 Modifications at KONTAS: recirculation line (orange), sampling station (green) and venting line (yellow) (Feulbach, 2024)

The goal of the project is to work towards examining the potential for regenerating hydrogen-loaded HCEs in already operational plants. This could be possible because the back-permeation of hydrogen from HCEs into the HTF can occur when no new

hydrogen is generated in the fluid. However, this regeneration is only feasible if the hydrogen partial pressure is kept at a very low level.

To ensure hydrogen removal from the system, both the hydrogen initially generated within the HTF and that absorbed in the HCEs must be released. For this purpose, a gas venting system was designed and installed at the KONTAS facility as seen in Figure 11. This system enables regular venting of the expansion tank, which is critical for maintaining low hydrogen levels.

To ensure that the hydrogen-loaded fluid in the loop mixes with the fluid in the expansion tank, and therefore enables outgassing of hydrogen, a custom recirculation line was incorporated. This allows HTF with high hydrogen load from the loop to mix with the HTF in the expansion tank, promoting the release of hydrogen into the vapor space within the tank. An additional bypass line at the recirculation line was also installed for sampling purposes. This line features two cylinders arranged in-line at an angle of 30° from horizontal, enabling the collection of HTF samples while KONTAS is operational, providing valuable data for monitoring the system's performance.

3.4.5 Gas composition inside the expansion tank

The upper part of the expansion tank contains a gaseous phase, primarily composed of nitrogen which is used instead of air to prevent corrosion. Additionally, there is also hydrogen in the headspace which constantly gases out from the HTF. This gaseous phase in the headspace enables selective venting of only the gases, avoiding the venting of the liquid. The nitrogen in the expansion tank can be easily replaced as needed, however, at a certain cost.

In the lower part of the tank is the liquid HTF. To ensure that the fluid in the expansion tank is constantly mixed with the fluid circulating in the loop and, therefore, equally loaded with hydrogen back-permeated from the HCEs, a custom recirculation line was installed between the loop and the expansion tank.

The recirculated fluid is sprayed through a pipe with holes to make sure the hydrogen is distributed as best as possible inside the gaseous upper part of the tank. The standard fill level of the fluid inside the expansion tank is approximately 30% at ambient temperature, with an increase to around 36 % at the observed maximum at approximately 375 °C due to thermal expansion of the fluid in the whole system.

4 Methodology

To evaluate the effectiveness of the hydrogen removal process, each step within the entire procedure must be analyzed. By dissecting the process, it becomes possible to identify critical factors influencing hydrogen reduction, assess any potential losses or inefficiencies, and optimize the sequence for maximum impact.

4.1 Steps of hydrogen removal and methods used to check their effectiveness

Step one involves the removal of hydrogen from the HCEs. This requires the partial pressure of hydrogen in the HTF to be lower than that in the vacuum annulus. To assess the effectiveness of this process, the hydrogen content within the annulus is measured both before the HCEs are installed and after their removal at the conclusion of the experiments.

The initial measurement is conducted in a laboratory before the HCEs are installed at KONTAS. This process cannot be repeated during the experiments as it requires laboratory conditions and the removal of the HCEs. The primary objective of this step is to determine the exact amount of hydrogen removed. While regular checks would be beneficial, the second measurement can only be performed once the project concludes, allowing for the HCEs to be disassembled and transported to the laboratory.

Since the required working hours at KONTAS to complete the project have not yet been achieved, this step falls outside the scope of the current work and will be addressed in the project's final stages.

In the second step, HTF from the loop is recirculated through the expansion tank, enabling hydrogen to transfer from the HTF to the gaseous phase inside the expansion tank. This process continues until equilibrium of partial pressure is reached. Although the effectiveness of hydrogen transfer from the HTF to the headspace gas in the expansion tank cannot be directly measured, it is assumed to be efficient due to the spraying of very hot HTF into the headspace gas. The recirculated mass flow is estimated using the time-of-flight method (see chapter 4.3.1 for details).

This step is the central focus of this work. To ensure effective hydrogen removal, the HTF in the loop - loaded with hydrogen diffused from the HCEs - must be consistently mixed with the HTF in the expansion tank. This mixing facilitates hydrogen outgassing into the gaseous phase. Measuring the volume of fluid pumped through the recirculation is crucial and must be conducted continuously. If the hydrogen partial pressure in the HTF becomes too high, further hydrogen removal from the HCEs is hindered.

In the third step, hydrogen is removed from the system by venting the gaseous phase inside the expansion tank. To evaluate the effectiveness of this process, samples of HTF are collected and sent to a laboratory for analysis. At the DLR laboratory in Cologne, Germany, the hydrogen content of these samples is determined, providing a

quantitative measure of how much hydrogen has been successfully removed from the system.

Analyzing all three steps of hydrogen removal helps identify which steps are sufficiently effective and which require more frequent or extended implementation.

4.2 Venting

This chapter outlines key considerations for venting, including necessary precautions, the influence of parameters, and the methods used to evaluate venting effectiveness. These works were carried out in advance of this thesis but are necessary to understand the execution of the experiments.

4.2.1 Condensation formation dependent on degassing temperature

To enhance fluid mixing for increased release of hydrogen into the headspace gas, recirculation through the expansion vessel should be maximized. However, in the current setup, this leads to tank temperatures of around 375°C. At such high temperatures, large quantities of low-boiling components from the HXLP fluid are present in the headspace gas and would be lost from the system during venting.

In a series of experiments, the relationship between tank temperature and the amount of vented HXLP was investigated. The system was heated to various temperatures, recirculated, and then vented while collecting and weighing the resulting condensate.

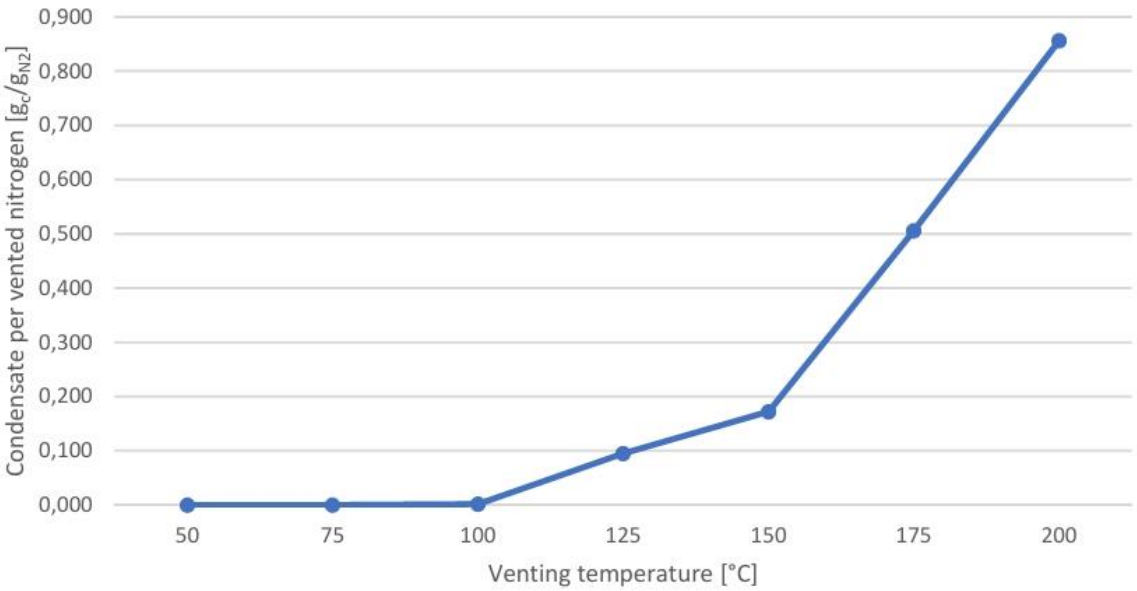

Figure 12 Visualization of the ratio of condensation mass to vented nitrogen mass at different temperatures (Feulbach, 2024)

As seen in Figure 12, at temperatures below 100 °C, condensate amounts were negligible. From 100 °C to 150 °C, the mass of vented condensate increased linearly,

and above 150 °C, the increase became more pronounced. At 200 °C, the condensate mass reached up to 0.856 g/gN_2.

As a result, venting at 150 °C was chosen as an optimal balance between minimizing fluid loss and reducing cooling time, which can take up to 16 hours when cooling from operating temperatures of around 375 °C.

4.2.2 Effectiveness of venting

As reported by (Feulbach, 2024), examinations were conducted prior to this thesis to assess the effectiveness of a single venting procedure in reducing hydrogen levels in the HTF. Fluid samples were collected both before and after the venting process to evaluate its impact. Initially, the system was operated for 24 hours under normal operating conditions, with recirculation occurring at a fluid temperature of 400°C. After opening the sampling line, HTF was circulated through two sample cylinders connected in series until the cylinder walls reached a stable temperature. The valves on the cylinders were then closed, and the samples were collected once they had cooled. Both sets of samples were sent to the DLR laboratory in Cologne for hydrogen concentration analysis via gas chromatography.

The analysis revealed a significant reduction in hydrogen concentration in the samples. Initial concentrations of around 1900 ppm in the two sample cylinders were reduced by approximately 40% after venting, to around 1100 ppm. Additionally, the methane (CH4) concentration was drastically lowered, although due to its larger molecular size, it is less likely to permeate into the vacuum region. According to internal DLR estimates, a hydrogen concentration well below 100 ppm is needed to enable back-permeation from the vacuum annulus into the HTF. Achieving further reductions in hydrogen levels would require more frequent venting (Feulbach, 2024).

4.3 Effectiveness of recirculation

To ensure that the fluid inside the loop and the expansion tank is constantly mixed and therefore the hydrogen can gas out into the gaseous phase inside the expansion tank, it needs to be determined how much fluid is pumped through the recirculation line. An easy and cheap solution to achieve this is the time-of-flight method.

4.3.1 Principle time of flight

Mass flow is derived using the time-of-flight method, which measures the delay in thermal response between two sensors. This delay is converted to fluid velocity, which is then used to compute both volume and mass flow rates. The basis of this measurement methodology is the measurement of a change in temperature. This change, whether an increase or decrease, is measured as a thermal step response at various sensors with a time delay. By analyzing the time offset between these step responses, the fluid velocity and consequently the volume flow and the mass flow are calculated.

During ongoing plant operations, monitoring the thermal step response offers an effective, cost-efficient method for system analysis. Unlike specialized sensors, such as mass flow meters, this approach leverages inexpensive temperature sensors that are often already installed throughout commercial PTC power plants. These existing sensors can capture temperature data, simplifying both installation and cost management.

Thermal step response, the basis of this method, can be induced by controlled thermal events. For instance, it may involve defocusing solar collectors or activating circulation before sunrise to create measurable temperature changes (Thomas Kraft et al., 2024).

In this work, the thermal step response is initiated by opening the recirculation line, allowing the 400 °C hot fluid from within the loop to flow through the recirculation line, which has cooled to ambient temperature. This sudden temperature increase from ambient to approximately 400 °C is then used to determine the time of flight.

Due to the short measurement distance of only 3.75 meters and because the recirculation is kept open and not just closed again after a short burst, it is not possible to use the same indicator as used by (Thomas Kraft et al., 2024), the maximum temperature. Instead, only the initial slope of the temperature increase can be utilized as an indicator to calculate the time.

The first step is to calculate the velocity *v* of the fluid by dividing the measured length difference between the temperature sensors Δl by the measured time difference Δt:

$$v = \frac{\Delta l}{\Delta t} \tag{1}$$

By using the cross-sectional area *A* of the pipe calculated by the circle number π and the pipe diameter *d*:

$$A = \frac{\pi}{4} * d^2 \tag{2}$$

And multiplying it with the velocity *v*, the volume flow $\dot{V}$ *is* calculated:

$$\dot{V} = v * A = \frac{\Delta l}{\Delta t} * \frac{\pi}{4} * d^2 \tag{3}$$

Using now the density ρ of the heat transfer fluid and multiplying it with the volume flow $\dot{V}$, the mass flow $\dot{m}$ is calculated:

$$\dot{m} = \dot{V} * \rho = v * A * \rho = \frac{\Delta l}{\Delta t} * \frac{\pi}{4} * d^2 \cdot \rho(\vartheta) \quad (4)$$

Whereby the density ρ is dependent on the temperature ϑ of the HTF, see Appendix B.

5 Operation and analysis

This chapter aims to detail the operational procedures and analytical methods employed during the experimental phase, highlighting the challenges encountered and the solutions implemented.

5.1 Blockages in venting line

During test runs repeated blockages occurred in the venting line. No gas exited the venting line to the atmosphere, prompting an inspection of the pipes. Upon opening the pipes, a solid material with an ice-like appearance was discovered, obstructing the flow.

This phenomenon can be attributed to the separation and solidification of light boiler components from the HTF when they came into contact with the cold surfaces of the venting line, which was at ambient temperature. While such blockages are highly unlikely during normal operations in commercial plants - where no hot gas containing dissolved light boilers comes into contact with cold surfaces, as the expansion tank does not heat up to 150 °C and more - this issue became relevant in this test setup.

To prevent future blockages, the venting line needs to be heated to a temperature above the highest solidifying point of all HXLP components. This was achieved using heat tracing with an electrically heated wire applied to the venting line. In addition, the safety and overpressure valve pipes are also heated now to prevent blockages in these safety-critical components.

5.1.1 Solidification of HTF: identifying the solidifying component

To address the issue of solidification in the HTF, it was necessary to determine which component of it solidifies and at what temperature this occurs. HXLP, the HTF in use, comprises various components, a detailed list of which is provided in Appendix A. From this table, three likely components were identified as potential causes of the observed solidification:

Hexamethyldisiloxane ($C_6H_{18}O_1Si_2$)
Abbreviated as Si_2, with a boiling point of 100°C and a melting point of -59°C.

Hexamethylcyclotrisiloxane ($C_6H_{18}O_3Si_3$)
Abbreviated as D_3, with a boiling point of 135°C and a melting point of 63–67°C.

Octamethylcyclotetrasiloxane ($C_8H_{24}O_4Si_4$)
Abbreviated as D_4, with a boiling point of 175°C and a melting point of 17–18°C.

Given that KONTAS operates at ambient temperatures above 20°C, Si_2 was ruled out due to its low melting point of -59°C, which is far below relevant operating conditions. D_4, with a melting point of 17–18°C, is a possible candidate but less likely than D_3. D_3,

with a melting point of 63 - 67 °C, was identified as the most probable solidifying component. However, both D_3 and D_4 are contaminated by other volatile components during operation, which likely lower their effective melting points. Consequently, while the exact melting point cannot be precisely predicted, an assumption was made that solidification may begin around 60 °C.

To prevent solidification, it is essential to ensure that the temperature in the affected areas does not drop below 60 °C. For added security, a margin of 10 °C was established, setting the minimum temperature at 70 °C. This can be achieved through heat tracing, which maintains the system above this critical temperature and ensures uninterrupted operation.

5.1.2 Analyzing design of venting line

To ensure the venting line operates efficiently and without unnecessary cooling, its current configuration was analyzed to identify any components that might enhance cooldown. A cooler, previously installed to promote condensation during earlier investigations, was identified as a source of excessive cooling. In the following, the cooler was removed from the venting line to eliminate its unwanted cooling effect, ensuring it does not contribute to the formation of blockages. Additionally, a barrel was integrated at the end of the venting line to collect any potential condensate, ensuring proper functionality without compromising the temperature maintenance.

The barrel was further equipped with a nitrogen line to purge any residual oxygen and hydrogen before initiating the venting process and introducing new hydrogen. This precaution was essential to mitigate the high risk of a hydrogen-oxygen explosion. Hydrogen and oxygen mixtures possess a remarkably wide flammability range and can react explosively with minimal energy input, such as a small spark, heat source, or static electricity. By purging the barrel with nitrogen, the presence of oxygen was effectively eliminated, ensuring safe operation and reducing the risk of flame or explosion during the venting process.

5.1.3 Heat tracing

The heat tracing system, also known as trace heating, at KONTAS was designed with specific requirements in mind to ensure its suitability for the venting line before installation. These requirements included compatibility with outdoor installation, necessitating dust and waterproof protection using mineral-insulated cables. The system was also required to operate electrically on 230 V alternating current and function reliably at temperatures up to 400 °C, aligning with the maximum operational temperature of the KONTAS test bench. These considerations ensured the trace heating system met all operational and environmental demands prior to its installation.

To optimize efficiency, additional insulation was applied to minimize electricity consumption and maintain a consistent temperature throughout the venting line. This was

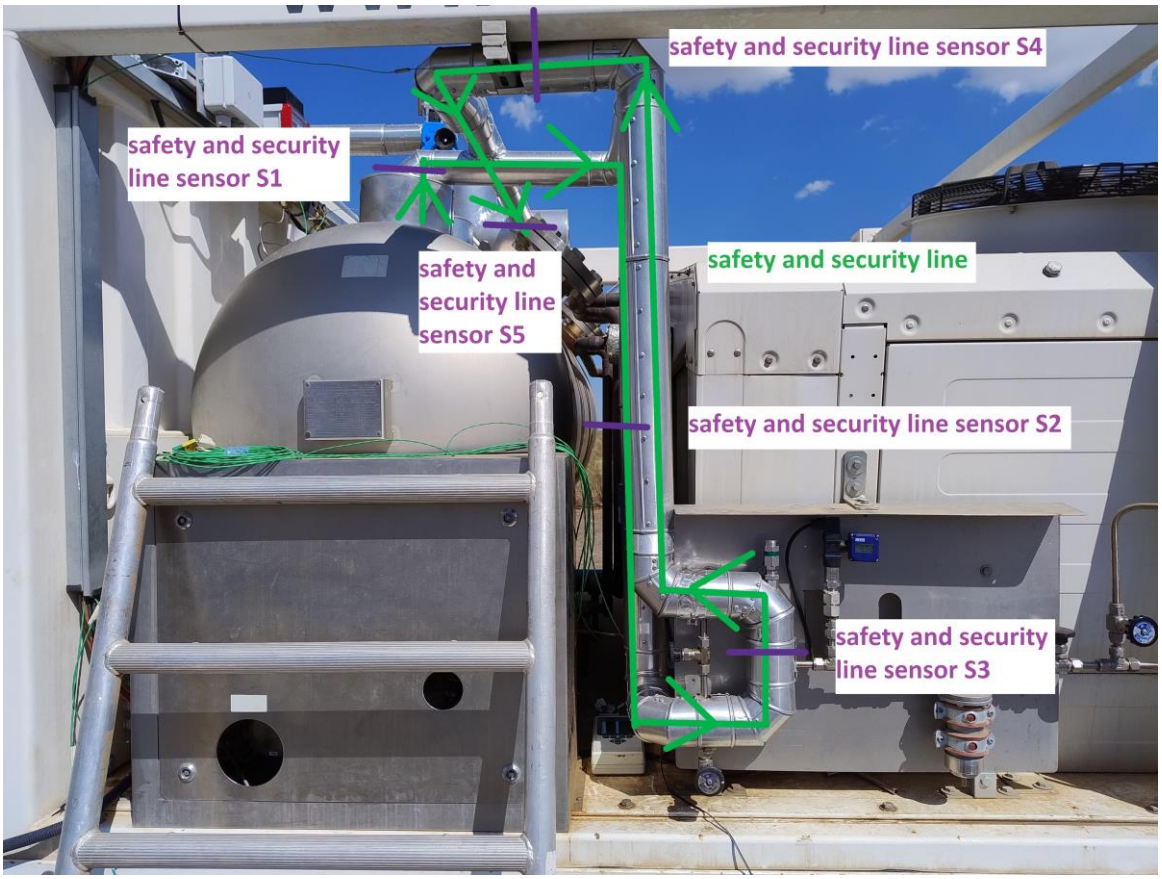

Figure 13 Temperature sensor positions at the safety and security valve line in side view

achieved by wrapping the line with mineral wool insulation, covered by sheet metal for weather protection. A controller supervises the trace heating system by comparing the actual temperature, measured by a type K thermocouple, with the set temperature.

Because the 15-meter-long trace heating line provides uniform power output, variations in environmental and operational conditions across the piping must be accounted for. Factors such as direct sunlight and proximity to the tank increase the temperature, whereas limited insulation in certain areas, due to space constraints or additional installations, leads to increased heat loss. Furthermore, components like the safety valve, which is larger compared to the 16 mm pipe, require more energy to heat and maintain temperature.

To ensure the entire line meets the minimum temperature requirement, the coolest point of each line had to be determined. Eight additional temperature sensors were strategically installed at critical points: three on the venting line (V3 near the barrel, V1 next to the expansion tank, and V2 in the middle of the line) and five on the safety and security valve line (S5 directly on the safety valve, S1 at the connection to the expansion tank, S3 at the point where the line connects to the nitrogen supply, and S2 and S4 in the two intermediate positions between these three sensors, whereas S4 was

additionally installed at a location where proper insulation could not be applied). All temperature sensor positions are shown in Figure 13, Figure 14 and Figure 15.

With these temperature sensors the coolest point on each line was determined and in consequence the sensor at this position connected to the controller. At the venting line, the sensor was positioned adjacent to the tank, while for the safety and security line, it was connected to the safety valve. In both cases, the heating process is extended due to the need to warm not only the line itself but also a large metallic structure, which requires significant energy and time to reach the needed temperature.

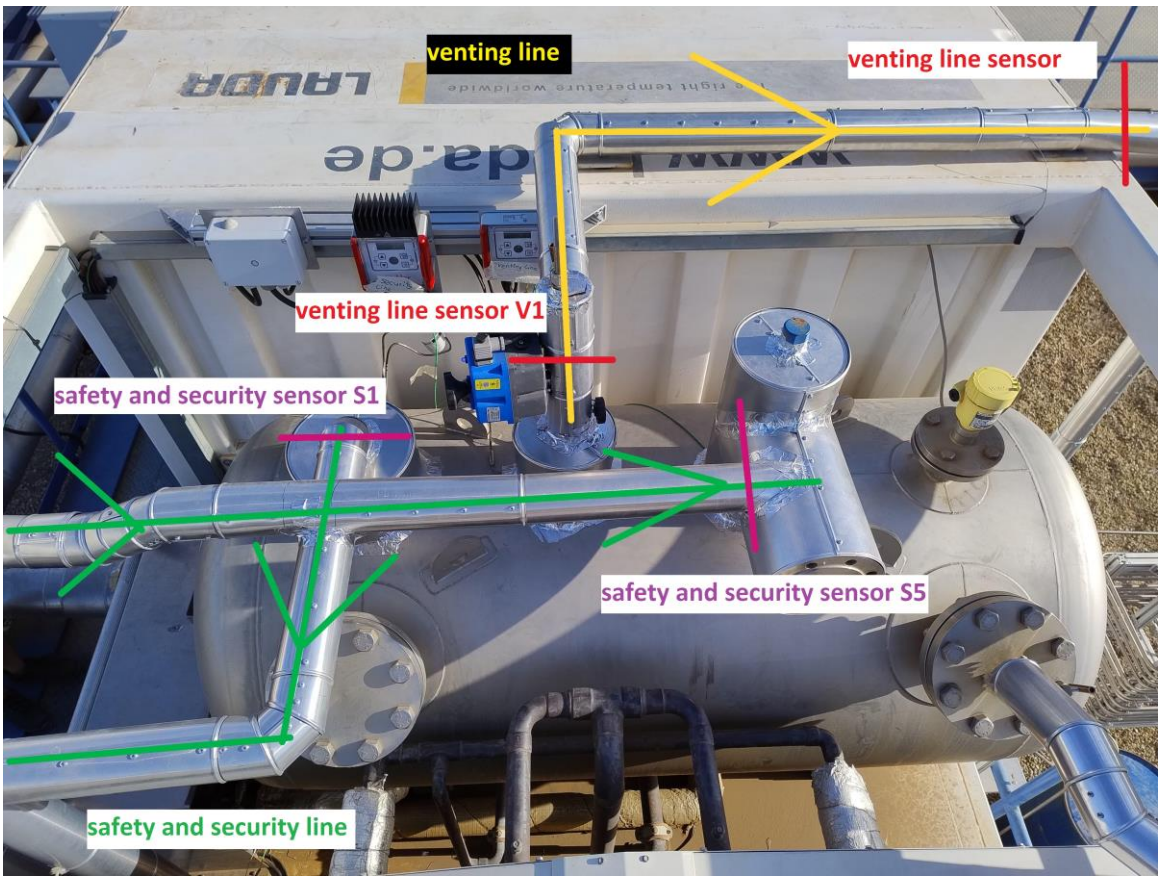

Figure 14 Top view on temperature sensor positions of both lines

Figure 15 Side view on temperature sensor positions of the venting line

5.2 Positioning of temperature sensors for time of flight

In order to carry out the time-of-flight measurement a pair of temperature sensors had to be installed at the recirculation line. The considerations regarding the installation of the sensors were the following:

1. The sensors need to be installed fast and easily to not cause a downtime of KONTAS.
2. The sensors need to be accessible for later adjustments and possible necessary repairs.
3. The distance between them needs to be as long as possible to improve measurement accuracy as it amplifies the time-of-flight differences, making minor variations in the speed of the temperature wave easier to detect over a greater distance.
4. While a longer measurement distance could increase sensitivity to external disturbances, the complete insulation of the setup and the large temperature difference between inflowing fluid and the cold recirculation line mitigates this risk by minimizing environmental influence.
5. The recirculation line exhibits varying diameters along its length. To simplify subsequent calculations, it is preferable for the pipe to maintain a consistent diameter over the measured distance for the time of flight.

At the time of the planned installation, two leaks occurred in the recirculation line, requiring the removal of the insulation. These two positions were nearly optimal in terms of the relevant considerations. To further save valuable operating time for KONTAS and minimize the work effort, these two positions were selected for the installation of the temperature sensors, see Figure 16.

For redundancy measure, two sensors were installed at each position to allow for a comparison of the temperatures at both sensors, thereby enhancing the accuracy of the measurement. Additionally, this setup prevents immediate replacement and, consequently, reduces downtime for cooldown across the entire test bench when a sensor malfunctions or stops working.

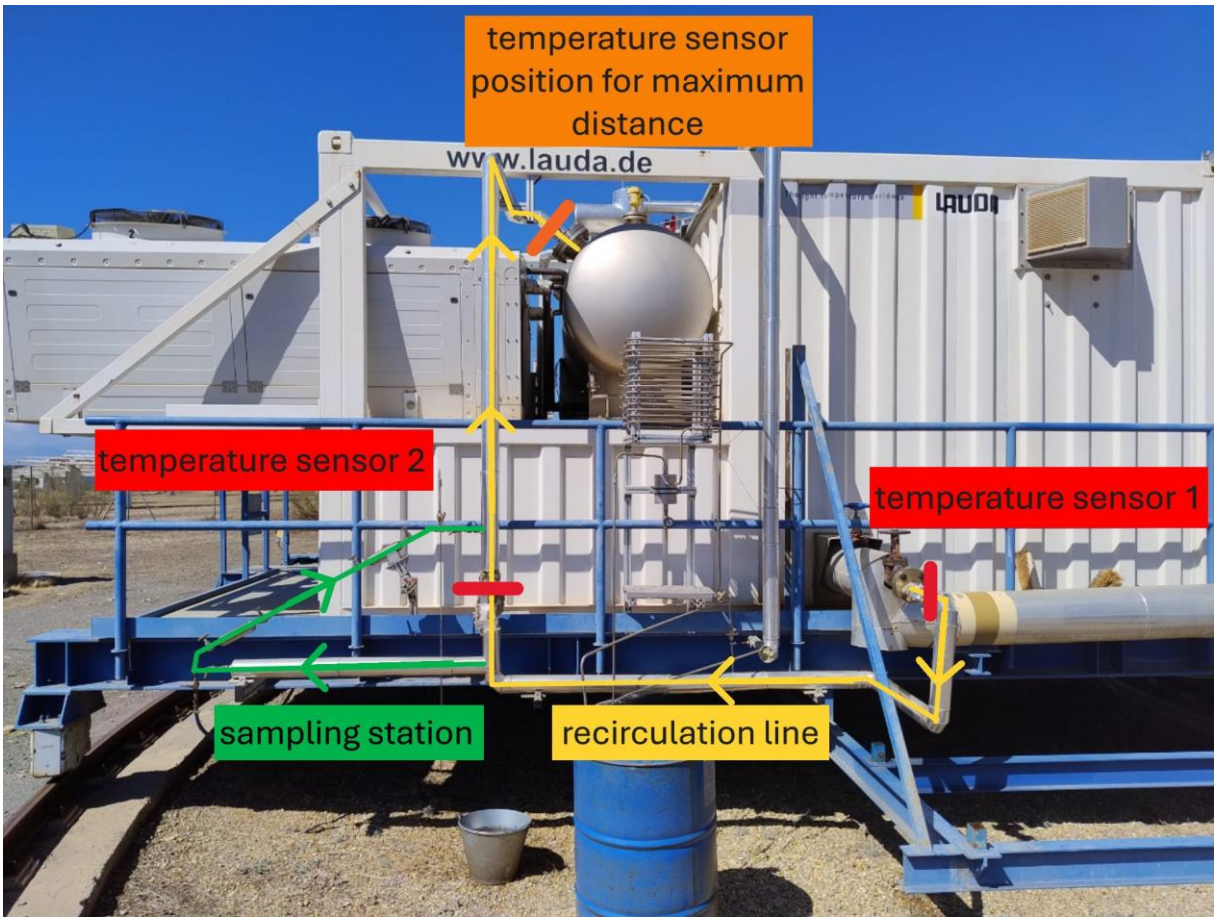

Figure 16 Temperature sensor positions at recirculation line

5.3 KONTAS operation parameters

The operation parameters for this experiment were designed to align with standard operation conditions found in commercial PTC power plants to ensure the findings are relevant to such systems. Achieving the highest possible efficiency, and therefore the highest feasible operating temperature, is a primary goal. The maximum allowable operating temperature of HXLP is above 425 °C. However, the KONTAS system is limited to a maximum temperature of 400 °C, which could also be achieved in existing plants running with DPO/BP.

According to the HXLP data sheet, operating at 400 °C corresponds to a vapor pressure of 10.33 bar (Figure 17). To maintain a safety margin, the system is typically operated above 10.5 bar. The system pressure is adjustable by introducing or releasing nitrogen into the headspace of the expansion tank, allowing precise control to meet operational and safety requirements. All pressure values in this thesis are presented in bar gauge (bar(g)), representing the pressure difference between the KONTAS system and atmospheric pressure.

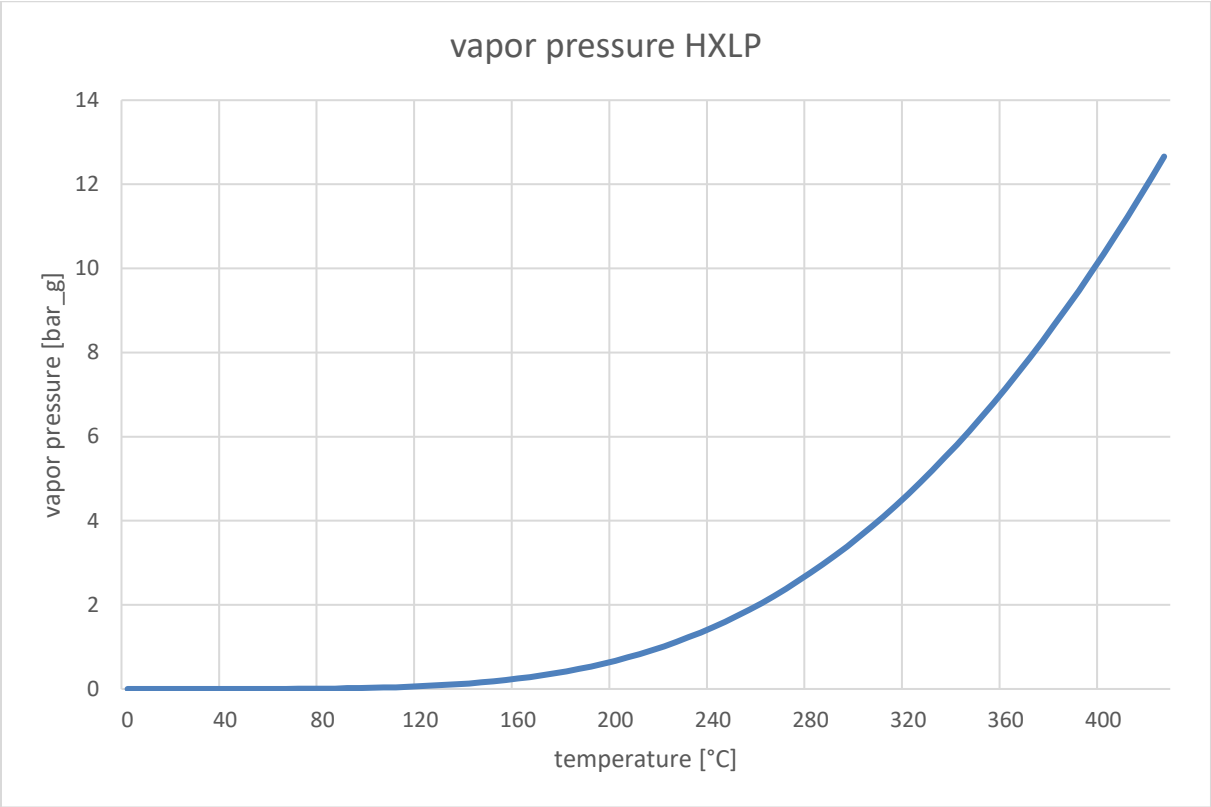

Figure 17 Vapor pressure HELISOL XLP over temperature; data from HXLP data sheet (Wacker Chemie AG, 2024)

5.3.1 Problem when opening the recirculation

Opening the recirculation during operation at 400 °C and 10,5 bar in the loop, with the expansion tank preheated to 150 °C, presents significant challenges. When the recirculation is opened, the significant temperature difference causes a rapid and immediate rise in pressure, quickly exceeding 14.5 bar within minutes. This triggers the overpressure switch, which is the first safety feature besides the overpressure and safety valves, causing the KONTAS system to shut down at 14.8 bar.

To restart, the pressure must be reduced to below 11.8 bar, followed by a manual reset of the system. This can only be achieved by venting at high temperatures, which is undesirable, or by waiting until the tank temperatures drop sufficiently, resulting in lost operational time. Opening the recirculation with these parameters is, therefore, impractical for continuous operation, prompting the implementation of an experimental pressure limit of 14.5 bar to prevent the overpressure switch from activating.

5.3.2 Investigation about rapid pressure rise

The rapid pressure increase upon opening the recirculation cannot be attributed to significant changes in the tank's filling level, as this varies by only 1 to 2%. Instead, the primary cause lies in the substantial temperature difference between the recirculated hot fluid at 400 °C and the cooler expansion tank at 150 °C.

This temperature difference leads to the thermal expansion of the gas in the expansion tank headspace. The nitrogen there heats up rapidly, causing its volume to expand and resulting in an immediate pressure increase.

To gain a deeper understanding of the pressure dynamics and determine the temperature at which the nitrogen exceeds the critical pressure of 14.5 bar, detailed calculations were performed.

The authoritative formula for solving this problem is the ideal gas equation

$$p \cdot V = R \cdot T \cdot m \tag{5}$$

First the mass of the nitrogen in the expansion tank headspace before the recirculation gets opened is calculated. Several values to solve that equation are already known:

The temperature in the expansion tank is 150 °C, the experimentally determined optimal venting temperature, because the amount of vented gaseous fluid at this temperature is tolerable.

An also known size is the system pressure of 10.5 bar. It is the vapor pressure of HXLP at 400 °C, plus a security margin to not fall below that threshold.

The next known value is the ideal gas constant for nitrogen R_{nitrogen} which is 296.8 J/kg·K.

Unknown is the volume of the nitrogen in the headspace of the expansion tank V_{nitrogen}. To determine that, the shape of the expansion tank is assumed to be a perfect cylinder. First the cross-sectional area of the cylinder A_{circle} is calculated.

The volume of a cylinder V_{cylinder} is calculated by

$$V_{\mathrm{cylinder}} = L_{\mathrm{cylinder}} \cdot A_{\mathrm{circle}} = L_{\mathrm{cylinder}} \cdot 2 \cdot \pi \cdot r_{\mathrm{circle}}^2 \tag{6}$$

Because only the volume of the nitrogen filled headspace is needed, the volume of the expansion fluid at the bottom of the tank needs to be subtracted. The area of a circle section A_{section} in a horizontal cylinder is determined by

$$A_{sec} = {r_{\mathrm{tank}}}^2 \cdot \arccos\left(\frac{r_{\mathrm{tank}} - h}{r_{\mathrm{tank}}}\right) - (r_{\mathrm{tank}} - h) \cdot \sqrt{2 \cdot r_{\mathrm{tank}} \cdot h - h^2} \tag{7}$$

With Eq. 6 converted to

$$r_{\text{tank}} = \sqrt{\frac{V_{\text{tank}}}{L_{\text{tank}} \cdot 2 \cdot \pi}} \tag{8}$$

and the volume of the whole expansion tank V_{tank} known to be 750 liter and an assumed tank length L_{tank} of 2 m, the radius of the tank r_{tank} is calculated to 0.3456 m.

The necessary filling height h is

$$h = 2 \cdot r_{\text{tank}} \cdot \Phi \tag{9}$$

With the calculated radius of the tank and the filling level Φ known to be 34%, the filling height is calculated as 0.235 m. Inserting r_{tank} and h into A_{sec} results in 0.1125 m².

The volume of the HTF in the expansion tank is in consequence the tank length L_{tank} multiplied with the area of a circle section $A_{section}$

$$V_{\text{HTF\_in\_tank}} = L_{\text{tank}} \cdot A_{\text{section}} \tag{10}$$

Inserting L_{tank} and $A_{section}$ in, the result is 0.225 m³.

To get the volume of the nitrogen $V_{nitrogen}$ the volume of the HTF in the tank $V_{HTF\_in\_tank}$ is subtracted from the volume of the whole expansion tank V_{tank}

$$V_{\text{nitrogen}} = V_{\text{tank}} - V_{\text{HTF\_in\_tank}} \tag{11}$$

Inserting results is 0.525 m³.

To calculate the nitrogen mass m, Eq. 5 is rearranged and the calculated values inserted, resulting in a value of 4.39 kg.

In the next step the maximum temperature before the nitrogen reaches 14.5 bar is calculated.

The ideal gas equation is rearranged to the temperature *T*, inserting the already known values and the to 14.5 bar changed pressure *p*, the result is 312 °C.

This means, to ensure the system pressure does not exceed 14.5 bar, the maximum allowable temperature of nitrogen in the expansion tank headspace is 312 °C.

However, due to the rapid heating of nitrogen compared to the HTF in the tank, this limit is likely to be surpassed. This discrepancy arises because the recirculation pipe delivers heat directly into the gaseous headspace, and nitrogen, with its lower heat capacity compared to HXLP, absorbs heat more quickly.

Given that the loop operates at 400 °C and the expansion tank temperature rises to approximately 375 °C, it is clear that the nitrogen temperature will exceed the 312 °C threshold and in consequence cause the pressure to surpass the 14.5 bar limit.

5.3.3 Adapting the recirculation procedure

The initial approach to addressing the rapid temperature and pressure increase in the headspace gas during recirculation was to minimize the mass flow into the tank. This was achieved by opening the recirculation hand valve to the minimum extent possible.

While this slows the rate of pressure increase and extends the recirculation time to 15 to 20 minutes before the 14.5 bar limit is reached, it remains a suboptimal solution. The limited recirculation time does not allow for sufficient mass circulation to ensure that the entire system mass is properly recirculated. Furthermore, the hand valve's lack of precision - due to its manual operation and age - results in irregular movement and reduced reliability, compromising consistent and reproducible control. Although this strategy has led to some improvement, achieving longer recirculation times is still both necessary and desirable for practical operation.

But there is one scenario where the KONTAS system operates below 400 °C: during the venting of the gaseous headspace of the expansion tank and refilling it with nitrogen in the morning. This procedure, which takes approximately 20 minutes, causes both the loop and the expansion tank to cool down. During venting, the 150 °C hot gas phase is released and replaced with nitrogen at ambient temperature, resulting in additional heat loss and some mixing of the cold HTF in the tank with the hot HTF in the loop.

Before restarting the pump, the recirculation is completely opened. The loop temperature at this point is approximately 300 °C. Referring to the vapor pressure graph in Figure 17, the pressure at 310 °C corresponds to 4 bar. Therefore, after venting, it is sufficient to refill the nitrogen to approximately 4 bar.

When the recirculation is reopened and the loop heats up to 400 °C, the pressure increases first rapidly due to the temperature increase in the headspace gas and then gradually to eventually stabilize at 12 bar to 13 bar at 400 °C. With this new approach, the system operates safely above the vapor pressure and continuous recirculation for an infinite amount of time is possible.

5.3.4 New procedure in detail

The standard operating parameters of the KONTAS system are defined as a loop temperature of 400 °C, an expansion tank temperature of 150 °C, and a system pressure of 11 bar.

Each morning, the system undergoes a venting process to remove the gases accumulated in the headspace of the expansion tank, to achieve the goal of removing most hydrogen from the headspace gas. Before venting, the valve in the nitrogen line that ensures that the pressure does not drop below 11 bar during the night is closed. The gas phase is then vented until the system pressure is reduced to 1 bar above ambient pressure, ensuring most of the gaseous headspace in the expansion tank is evacuated. Maintaining this pressure difference prevents ambient air from entering the system, which would otherwise lead to corrosion. After venting, nitrogen is refilled into the system until the pressure reaches 4 bar.

Before restarting the system, the recirculation valve is fully opened. After restarting, the fluid in the loop and in the expansion tank begin to mix. The temperature sensor for the loop temperature is approximately at that position located, where the fluid from the expansion tank enters the loop. In consequence the shown loop temperature after restart drops to approximately 300 °C and the one in the tank rises to 180 °C. The system continues recirculating throughout the day. During that, the loop temperature reaches 400 °C and the temperature in the tank increases to around 375 °C .

In the afternoon, the recirculation valve is closed as part of the preparations for the overnight operation. The loop temperature is still set to 400 °C, and the expansion tank temperature to 150 °C. But because no fluid from the loop is recirculated anymore, this allows the tank to cool down overnight to 150 °C, thus preparing it for the venting process the following day. To prevent the system pressure from dropping below 11 bar, the nitrogen pressure reducer is set to keep the pressure above that threshold.

5.3.5 HTF samples

The objective of sampling is to evaluate the concentration of hydrogen in the HTF to assess whether the current venting procedure is adequate or if more frequent venting is necessary.

When samples are taken, the recirculation stream is bypassed through the sampling station. The recirculation is kept open until the sample containers are completely warmed up to the HTF temperature of 400 °C. Thus, it is ensured that all samples are taken under the same conditions. Once the sampling is completed, the recirculation is closed completely to prepare the system for overnight operation.

Over the course of the study, one set of samples was sent to Cologne for laboratory analysis. Samples were collected on five different days, with two containers taken per day. For each sample, key parameters were recorded, including the temperature

(400°C), system pressure (11–12 bar), whether the container was installed upstream or downstream, and the composition of the fluid (HXLP with 2% VP-1).

By the conclusion of this thesis, no results had yet been received from the laboratory, leaving the analysis of the hydrogen concentration incomplete.

5.4 Data analysis

This chapter discusses the process of data logging, visualization, and analysis. It covers the calculation of time of flight, mass flow, and the resulting recirculated mass, along with their associated uncertainties.

5.4.1 Recorded data

The data for this experiment was recorded using two primary systems: the Ahlborn Almemo 2890-9 logger and the automated recording of data (from the PLC integrated in KONTAS) with LabView. The Ahlborn Almemo 2890-9 logger, capable of handling up to 8 channels, was used to measure temperature over time along the recirculation line. Four thermocouple type K sensors were deployed, positioned at two locations along the measurement section, with two sensors placed at the start and two at the end of the section.

In addition, the KONTAS system, operating through LabView, automatically recorded data every day at midnight in an Excel sheet. The parameters logged included time, loop temperature, system pressure, and mass flow. However, the expansion tank temperature was not integrated into the LabView system and therefore was not automatically saved. This parameter was only accessible via the interface directly on the HCU system.

5.4.2 Calculating time of flight

The calculation of the time of flight was based on temperature data recorded by the four sensors at the two positions along the recirculation line, using the Ahlborn logger. This data was transferred to a laptop via USB cable and stored in an Excel file, where it was visualized in graph form for initial inspection. A visual check was conducted to identify anomalies, such as missing signals from sensors, incorrect data (e.g., ambient temperature readings on a line with 400 °C hot fluid), or inconsistencies between the two signals at the same position. In cases where signals from the same position appeared significantly different and did not share a similar shape, these were flagged as errors.

Maximum temperatures and the highest slopes recorded between positions 1 and 2 were rarely identical, due to heat losses between the two positions. Measurements at position 2 consistently showed a slower incline, due to thermal inertia of the system, as exemplary shown in Figure 18. Occasionally, two maxima were detected at position 2. This phenomenon was likely caused by the HTF in the insulated pipe between the two positions cooling more slowly than the fluid directly at the non-insulated sensor

locations. When the recirculation was opened, the still warm HTF was pushed through to position 2, resulting in a first peak. The second peak is reached once the hot HTF from the main loop reaches the sensor.

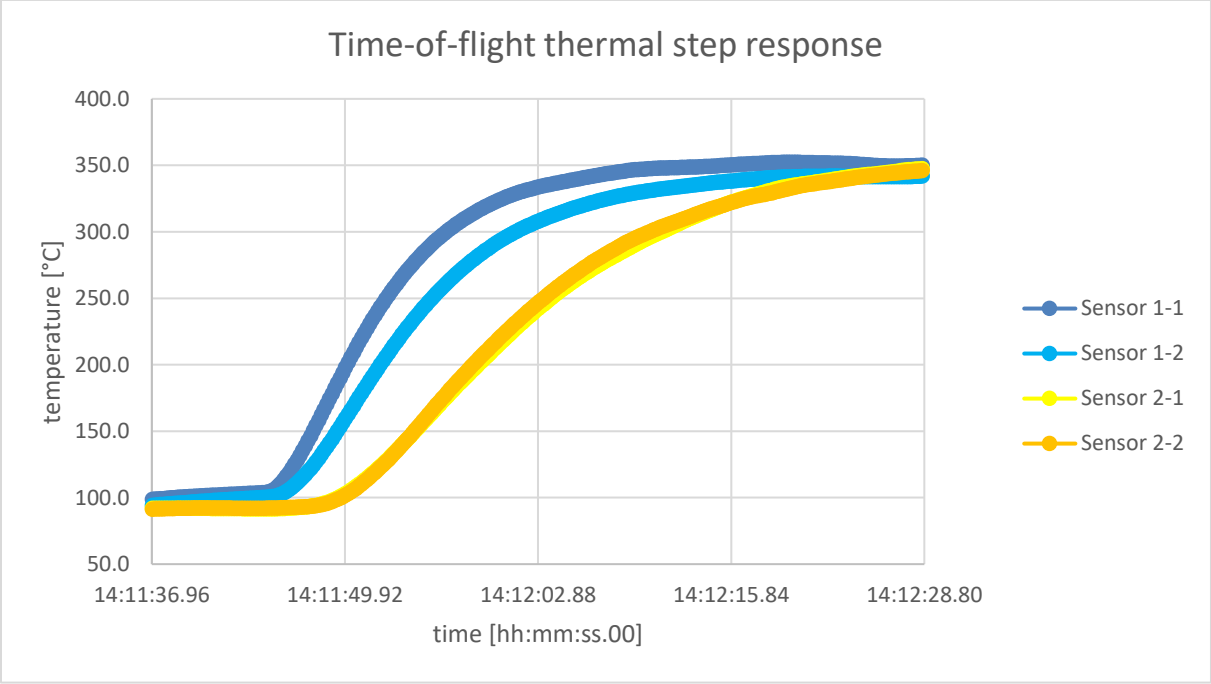

Figure 18 Exemplary thermal step response to determine the time-of-flight

The steepness of the temperature rise depended on the initial state of the recirculation line. If the line was not completely cooled to ambient temperature, the temperature rise was less pronounced, making it more challenging to identify the exact moment of opening. Optimal results were achieved when the line was cooled completely to ambient temperature (20–30°C), creating the greatest temperature difference compared to the 400°C loop temperature.

To address temperature jumps caused by sensor inaccuracies, the graphs were smoothed by averaging three values. Although experiments with smoothing windows of 5, 10, and 20 values were conducted, larger windows significantly delayed the response time, rendering them unsuitable.

The first derivative of the temperature data was calculated to analyze the slope, using the difference between consecutive values. These derivative values were visualized to assess their reliability. A function was implemented in Excel to automatically detect the moment of temperature rise, with a threshold set to a minimum temperature increase of 0.2 K within 0.18 seconds. The threshold was confirmed stable when at least five consecutive values exceeded it.

To further reduce sensor inaccuracies, the average of the two sensors at the same position was calculated. The time of flight was then determined as the difference

between the averaged values at the two positions. This process was repeated for six sets of data, and the results were compiled in Table 1. Finally, the mean value of the six calculated time-of-flight values was computed, yielding an average time of flight of 0.51 seconds.

	26.09.24	26.09.24	27.09.24	30.09.24	03.10.24	03.10.24
Sensor 1 position 1 [hh:mm:ss.00]	15:34:43.37	15:54:58.91	15:06:22.77	15:43:40.27	13:23:48.35	14:51:57.67
Sensor 2 position 1 [hh:mm:ss.00]	n/a	n/a	15:06:23.31	15:43:40.63	n/a	14:51:58.03
Average position 1 [hh:mm:ss.00]	15:34:43.37	15:54:58.91	15:06:23.04	15:43:40.45	13:23:48.35	14:51:57.85
Sensor 2 position 1 [hh:mm:ss.00]	15:34:43.73	15:54:59.81	15:06:23.67	15:43:40.81	13:23:49.07	14:51:58.57
Sensor 2 position 2 [hh:mm:ss.00]	15:34:43.73	15:54:59.45	15:06:23.49	15:43:40.63	13:23:48.89	14:51:58.21
Average position 2 [hh:mm:ss.00]	15:34:43.73	15:54:59.63	15:06:23.58	15:43:40.72	13:23:48.98	14:51:58.39
Time of flight [mm:ss.00]	00:00.36	00:00.72	00:00.54	00:00.27	00:00.63	00:00.54

Table 1 Summary of the timestamps of temperature increases detected by two sensors during daily ToF experiments. The ToF was calculated as the difference between the average times for each sensor

5.4.3 Calculating recirculated mass

The automated data recorded via the KONTAS system relevant for this work are time, temperature, and mass flow values. Furthermore, the density at each recorded time point was calculated based on the corresponding temperature. This calculation relied on the HTF datasheet in Appendix B, which provides density values for specific temperatures, and linear interpolation.

This calculation was particularly necessary because the loop temperature—and consequently the recirculation line temperature—did not consistently remain at 400°C. For instance, after system malfunctions during the night that led to a shutdown, when the testbench was turned off during repairs and maintenance or when the recirculation line was reopened in the morning following venting, temperature variations were common.

Detecting whether the recirculation status was open or closed posed challenges, requiring combined criteria like mass flow above 4 kg/s and minor temperature fluctuations between the loop and expansion tank. However, these indicators were not always clear in the recorded data, making it too complex for a fully automated function. In some cases, no mass flow signal was available, necessitating manual entries based on the manual KONTAS Excel protocol. For these instances, recirculation status was recorded as “0” for closed and “1” for opened.

The mass flow at every time step (5 seconds) was calculated by multiplying the volumetric flow, which was assumed to be constant at the value calculated in chapter 4.3.1, with the fluid density. These values were then summed up over the entire day to determine the total recirculated mass.

Date [dd.mm.yyyy]	Time recirculated [min]	Total mass [kg]	Remarks
25.09.2024	253	8800	Normal operation
26.09.2024	268	9276	Normal operation
27.09.2024	151	5496	Outlier due to extended ToF tests
30.09.2024	255	9453	Normal operation
01.10.2024	268	9974	Normal operation
02.10.2024	301	10142	Normal operation
03.10.2024	311	10616	Normal operation

Table 2 Daily recirculated mass during experimental runs. The data includes anomalies, such as the 27.09.24 outlier, excluded from average calculations

When comparing these daily totals, as displayed in Table 2, six of the seven analyzed days exhibit consistent values ranging from 8,800 kg to 10,616 kg respectively 253 min to 311 min. However, the total recorded on 27.09.2024, 5,496 kg, and the associated time with only 151 min is a notable outlier. This lower value resulted from seven time-of-flight measurements conducted that afternoon, which led to the prolonged closure of the recirculation line.

As this scenario does not reflect typical operating conditions, the value was excluded from the average calculation, leading to a representative daily average of 9,710 kg. Taking into account that the total HTF mass in the system is only 665 kg, this implies that the entire fluid is recirculated more than 14 times per day.

5.4.4 Measurement uncertainties

Every experimental setup is subject to uncertainties, which must be carefully analyzed and documented to ensure the reliability and accuracy of the results.

Temperature Measurement

Temperature was measured using Type K thermocouples, classified as Class 1. According to the manufacturer TC Ltd. these sensors provide an accuracy of $\pm$1,5°C within the range of -40°C to +375°C. At higher temperatures, from 375°C to 1000°C, the tolerance increases to $\pm 0.004 \cdot |t|$, where |t| represents the measured temperature in degrees Celsius (TC Ltd., 2024). This specification means that the measurement uncertainty rises with increasing temperature.

The temperature logger, manufactured by Ahlborn, recorded the data submitted from the temperature sensors with a resolution of 0.1 K. To ensure the accuracy of the temperature sensors, calibration was conducted and involved measurement at

temperatures from 25°C to 400°C in 25°C increments. The entire process took one day to complete, covering all four sensors simultaneously.

However, several malfunctions of temperature sensors arose during operations. This led to repeated replacements of sensors and cables, as well as the discovery of a malfunction in one of the ports of the Ahlborn logger, which was subsequently not used anymore. After these changes, the remaining sensors produced consistent readings that fell within acceptable ranges, and they were deemed reliable. Due to time constraints, and since the absolute temperature values are not relevant for the time of flight method, recalibration was not performed to avoid further delays in the experiments.

Time Resolution

The Ahlborn logger has a time resolution $t_{resolution}$ of ± 0.18s, which represents the maximum possible accuracy of the equipment. Because the measured time of flight values are in a range below one second, such a low resolution introduces a substantial uncertainty in determining precise event timings.

Distance Between Sensors

The distance between sensors was measured manually using a meter stick. The recorded distance was 3.75m, with an estimated measurement uncertainty of ± 0.05m. Although this manual approach introduced a degree of variability, the tolerances were deemed sufficient for the experiment's requirements.

Pipe Dimensions

The pipe used in the setup had an outer diameter of 16mm and an inner diameter of 13mm. Both measurements carried a tolerance of ± 0.3mm. For the calculation of the cross-sectional area the inner diameter was used.

Time of flight

To calculate the total uncertainty of the time of flight $\triangle t_{\mathrm{ToF}}$ first the mean value $\overline{t_{ToF}}$ is calculated by dividing the sum of all values $\sum t_i$ by the sample size n by using

$$\overline{t_{ToF}} = \frac{\sum t_i}{n} \tag{12}$$

For the 6 samples defined in Table 2 under normal operation the mean value $\bar{t}$ is equal to 0.51 seconds.

Determining the standard derivation σ with

$$\sigma = \sqrt{\frac{\sum(t_i - \overline{t_{ToF}})^2}{n-1}} \tag{13}$$

To 0.17 seconds and inserting in the formula for the standard error of the mean value

$$SEM = \frac{\sigma}{\sqrt{n}} \tag{14}$$

The result is 0.07 seconds.

Inserting all calculated and known values in formula for the total uncertainty

$$\triangle t_{\mathrm{ToF}} = \sqrt{SEM^2 + t_{resolution}{}^2} \tag{15}$$

The result is 0.19 seconds. The complete measurement result for the time of flight is therefore $0.51 \pm 0.19\,\mathrm{seconds}$. The uncertainty of 37.3% is comparable high, but this is acceptable for this work, because it is a cheap and easy solution without interference in operations.

Density

The absolute measurement uncertainty of the density $\triangle \rho$ is calculated at 400 °C, where the density ρ is 536 kg/m³. This value is interpolated using the table in Appendix B. Because no uncertainty for the experimentally determined table is given, as conservative estimation a percentage error *PE* of 0.5% is used. In consequence the uncertainty for this from the table taken value is determined with

$$\triangle \rho_{\mathrm{Tab}} = \rho \cdot PE \tag{16}$$

to 2.7 kg/m³.

Because the used temperature is also measured and therefore underlies uncertainties, the associated uncertainty is

$$\triangle \rho_T = \left|\frac{d\rho}{dT}\right| \cdot \triangle T \tag{17}$$

With

$$\frac{\mathrm{d}\rho}{\mathrm{d}T} = \frac{\rho(T_{high}) - \rho(T_{\mathrm{low}})}{T_{high} - T_{\mathrm{low}}} \tag{18}$$

And

$$\triangle T = 0.004 \cdot |t| \tag{19}$$

Inserting the temperature t with 400 °C, T_{high} with also 400 °C, T_{low} with 390 °C, $\rho(400\,°C)$ with 536 kg/m³ and $\rho(390\,°C)$ with 557 kg/m³ the temperature measurement uncertainty results in 3.4 kg/m³.

Combining all density uncertainties with

$$\triangle \rho = \sqrt{(\triangle \rho_{Tab})^2 + (\triangle \rho_T)^2} \tag{20}$$

The complete density uncertainty $\triangle \rho$ results in 4.3 kg/m³. The complete measurement result for the density at 400 °C is therefore $536\ \mathrm{kg/m^3} \pm 4.3\ \mathrm{kg/m^3}$.

Velocity

The uncertainty for the velocity $\triangle v$ is determined by

$$\triangle v = \sqrt{\left(\frac{\triangle l}{l}\right)^2 + \left(\frac{\triangle t}{t}\right)^2} \cdot v \tag{21}$$

Inserting the velocity v, the time of flight t_{ToF} and its uncertainty $\triangle t_{\mathrm{ToF}}$, the length *l* and its uncertainty $\triangle l$ results in 2.74 m/s. The complete measurement result for the velocity *v* is therefore $7.35\ \mathrm{m/s} \pm 2.74\ \mathrm{m/s}$.

Volume flow

The uncertainty for the volume flow $\triangle \dot{V}$ is determined by

$$\triangle \dot{V} = \sqrt{\left(\frac{\triangle v}{v}\right)^2 + \left(2 \cdot \frac{\triangle D}{D}\right)^2} \cdot \dot{V} \tag{22}$$

Inserting the volume flow $\dot{V}$, the velocity *v* and its uncertainty $\triangle v$, the diameter D and its uncertainty $\triangle D$ results in 0.4 L/s. The complete measurement result for the velocity v is therefore $1.0 \pm 0.4\ L/s$.

Mass flow

The uncertainty for the mass flow $\triangle \dot{m}$ is determined by

$$\triangle \dot{m} = \sqrt{\left(\frac{\triangle \dot{V}}{\dot{V}}\right)^2 + \left(\frac{\triangle \rho}{\rho}\right)^2} \cdot \dot{m} \tag{23}$$

Inserting the mass flow $\dot{m}$, the volume flow $\dot{V}$ and its uncertainty $\triangle \dot{V}$, the density ρ and its uncertainty $\triangle \rho$ results in 0.20 kg/s. The complete measurement result for the mass flow $\dot{m}$ is therefore 0.52 kg/s $\pm$ 0.20 kg/s.

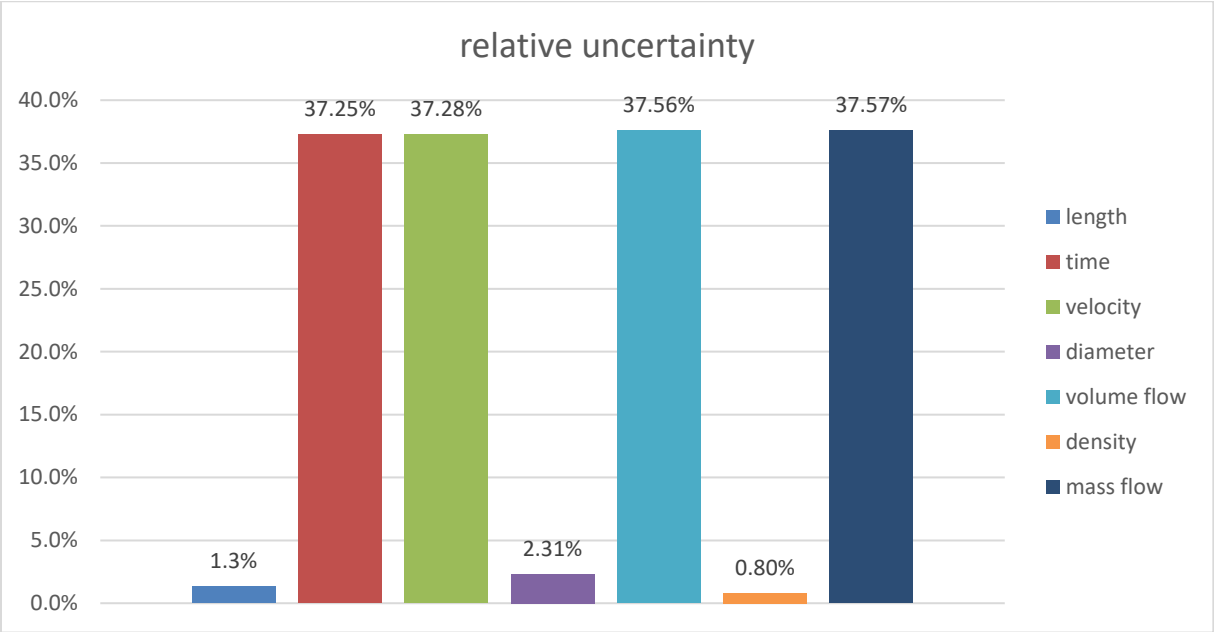

Figure 19 Relative uncertainties of all parameters required for calculating the mass flow

The relative uncertainties of all parameters necessary to calculate the mass flow are illustrated in Figure 19, arranged sequentially from the first for calculations used parameter on the left to the mass flow on the right. It is evident that the largest uncertainty, at 37.25%, is associated with the time measurement.

The subsequently calculated values - velocity, volume flow, and mass flow - show only a slight increase in uncertainty, culminating in 37.57% for the mass flow. This highlights that the time measurement has, by far, the greatest impact on the overall uncertainty, making it the most critical parameter in the calculation.

5.5 Possible new procedure

Based on the calculated minimum mass flow of 0.32 kg/s, it takes approximately 34 minutes to recirculate the entire 665 kg of fluid in the system. This information taken in account, a new daily operational procedure for hydrogen removal and recirculation was developed. The steps are as seen in Table 3:

Daytime	Description
9:00am	The day begins with venting the expansion tank, reducing pressure from approximately 11.5 bar to 1 bar, followed by refilling with nitrogen to 4 bar.
9:20am	The recirculation line is fully opened before restart of the pump, initiating the complete recirculation of the HTF, which takes 34 minutes according to the prior carried out calculations. The loop temperature drops to approximately 300 °C

	and the tank temperature rises to 180 °C within a few minutes.
10:00am	The recirculation line is closed, and the expansion tank temperature is observed to reach approximately 200 °C. Cooling of the tank begins while the loop continues normal operation at 400 °C.
3:00pm	After sufficient cooling, the expansion tank temperature is cooled down again to 150°C. Venting is performed again to reduce the pressure from 12 bar to 1 bar, followed by nitrogen refilling to 4 bar, taking another 20 minutes.
3:20pm	The recirculation line is reopened, and the entire fluid is recirculated again, completing the process at 4:00 PM.
4:00pm	The recirculation line remains closed during the night, allowing the loop to operate at 400°C for 17 hours. This high-temperature operation facilitates the removal of hydrogen from the vacuum inside the receiver tubes.

Table 3 Possible new procedure for recirculation and venting to enable venting twice a day described in detail

By following this schedule, it is possible to perform two complete recirculation cycles with venting per day, optimizing hydrogen removal. At the end of this thesis, it was not possible to test this new procedure anymore.

Evaluating the new operational procedure, it is crucial to additionally consider the currently unknown point at which the gaseous headspace of the expansion tank becomes saturated with H_2. Hydrogen in the HTF diffuses into the gaseous headspace during recirculation through the tank.

This process depends on the hydrogen partial pressures in both the HTF and the gaseous headspace. However, no investigations on this topic were conducted within the scope of this thesis. Consequently, the duration required to keep the recirculation open for headspace saturation remains unclear. To address this knowledge gap, future studies should include the collection and analysis of gas samples.

6 Conclusion and prospect

In this work, the operating procedure for a long-term experiment on hydrogen removal from solar thermal collector tubes was investigated. Removal of hydrogen includes three steps: transport from the absorber tubes' vacuum insulation into the fluid, from the fluid into the headspace gas of the expansion vessel and venting of the gas into the atmosphere. To enable effective and efficient removal, all three steps should occur at a similar speed.

The mass flow rate of the recirculated HTF through the expansion tank was determined using time-of-flight measurements. The results were subject to significant uncertainties due to the noninvasive installation of sensors and the limited temperature resolution of the data logger. Despite these limitations, an estimation of the order of magnitude, which was deemed sufficient for conducting the demonstration, was achieved.

The analysis of the measured data showed that the recirculation of the entire fluid in the system is feasible within a maximum of 34 minutes, indicating that recirculation is likely not a limiting factor and could be repeated several times per day. A change in operational procedure allows for continuous recirculation within the pressure limitations of fluid and system.

The effectiveness of hydrogen permeation from the absorber tubes into the HTF could not be assessed within this study as the remaining hydrogen content will only be measured ex-situ after conclusion of the experiment.

During the course of operation, several adjustments had to be made to the system due to unforeseen effects. For example, operation had to be interrupted several times because of blockages in the gas venting lines. These were caused by solidified low-boiling components of the HTF, which can occur when hot gas is exposed to cold surfaces. To avoid this, heat tracing lines were installed on the venting line and on critical safety equipment. Its effectiveness was confirmed by temperature measurements on the lines.

To advance the understanding of the system and help assess the possibility of hydrogen removal from contaminated tubes, further investigations are required. The hydrogen saturation level in the headspace gas of the expansion tank needs to be determined through the analysis of collected gas samples.

Moreover, analyzing HTF samples will quantify the amount of hydrogen removed from the fluid during venting. Finally, the hydrogen load in the receiver tubes will be evaluated after completing the entire experiment, offering a more comprehensive understanding of the system's performance and the limitations of hydrogen removal via venting.

7 Nomenclature

CIEMAT: Centro de Investigaciones Energéticas, Medioambientales y Tecnológicas

CSP: Concentrating solar power

DLR: Deutsches Zentrum für Luft- und Raumfahrt

HCE: Heat collecting element

HCU: Heating and cooling unit

HTF: Heat transfer fluid

HXLP: HELISOL XLP

KONTAS: KONzentrator Teststand Almeria Spanien

PB: Power block

PSA: Plataforma Solar de Almería

PTC: Parabolic trough collector

PV: Photovoltaics

SCA: Solar collector assembly

TES: Thermal energy storage

8 List of references

Abdul Hai Alami et. al. (2023). Concentrating solar power (CSP) technologies: Status and analysis.

ARANER. (2024). Von https://www.araner.com/blog/discover-the-three-types-of-thermal-energy-storage-systems abgerufen

BMWK. (24. 08 2024). Von https://www.bmwk.de/Redaktion/DE/Pressemitteilungen/2024/07/20240705-klimaneutrale-stromerzeugung-kraftwerkssicherheitsgesetz.html abgerufen

C. Jung et al. (2019). *Hydrogen monitoring in the heat transfer fluid of parabolic trough plants.* Cologne.

C. Jung et al. (2014). *Technological perspectives of silicone heat transfer fluids for concentrated solar power.* SolarPACES.

Chethan R. Reddy et al. (2018). *MODELING AND OPTIMAL CONTROL OF MICRO-CSP AND A BUILDING HVAC SYSTEM TO MINIMIZE ELECTRICITY COST.*

Christoph Hilgert et al. (2019). *Qualification of Silicone Based HTF for Parabolic Trough Collector Applications.* AIP Publishing.

D3. (20. 09 2024). *fishersci*. Von https://www.fishersci.com/store/msds?partNumber=AC216460250&productDescription=HEXAMETHYLCYCLOTRISILOXA+25GR&vendorId=VN00032119&countryCode=US&language=en abgerufen

D4. (20. 09 2024). *fishersci*. Von https://www.fishersci.com/store/msds?partNumber=AC216475000&productDescription=OCTAMETHYLCYCLOTETRASILOXANE&vendorId=VN00032119&countryCode=US&language=en abgerufen

Dow Chemical Company. (1997). *Dowtherm A Heat Transfer Fluid. Product Technical Data.*

Feulbach, M. (2024). *Experimental investigation of hydrogen reduction in PTC receivers by back-permeation into HELISOL® XLP silicone based HTF with accompanying venting of the HTF .*

Glatzmaier, G. (2019). *Hydrogen Mitigation Project.*

global solar atlas. (29. 08 2024). *global solar atlas*. Von https://worldbank-atlas.s3.us-east-1.amazonaws.com/download/World/World_DNI_mid-size-

map_160x95mm-300dpi_v20240530.png?X-Amz-Algorithm=AWS4-HMAC-SHA256&X-Amz-Content-Sha256=UNSIGNED-PAYLOAD&X-Amz-Credential=ASIAS2HACIWTFS5FCOUY%2F20241130%2Fus-east-1%2Fs3 abgerufen

H. Price et al. (2006). *Field Survey of Parabolic Trough Receiver Thermal Performance.* Denver, Colorado.

H.L. Zhang et. al. (2012). Concentrated solar power plants: Review and design methodology.

IEA. (2010). *Technology Roadmap Concentrating Solar Power.*

IEA. (2019). Von https://www.iea.org/commentaries/more-of-a-good-thing-is-surplus-renewable-electricity-an-opportunity-for-early-decarbonisation abgerufen

IEA. (2019). Von https://www.iea.org/reports/solar-energy-mapping-the-road-ahead abgerufen

IEA. (2023). Von https://www.iea.org/energy-system/renewables/solar-pv abgerufen

IEA. (2023). Von https://www.iea.org/reports/renewables-2023/executive-summary abgerufen

IEA. (2023). Von https://www.iea.org/news/the-energy-world-is-set-to-change-significantly-by-2030-based-on-today-s-policy-settings-alone abgerufen

Jibran Khan, M. H. (2015). Solar power technologies for sustainable electricity generation – A review.

Li et. al. (2012). Hydrogen permeation model of parabolic trough receiver tube.

NREL. (2022). Von https://solarpaces.nrel.gov/ abgerufen

Padilla, R. V. (2011). *Simplified Methodology for Designing Parabolic Trough Solar Power Plants.* Tampa: University of South Florida.

Pitz-Paal, R. (2020). *Concentrating Solar Power.*

REEEM. (2017). Von https://www.reeem.org/uploads/Pablo-Ralon-IRENA.pdf abgerufen

Si2. (20. 09 2024). *fishersci*. Von https://www.fishersci.com/store/msds?partNumber=AC194790100&productDescription=HEXAMETHYLDISILOXANE+98+10ML&vendorId=VN00032119&countryCode=US&language=en abgerufen

TC Ltd. (16. 10 2024). Von https://www.tc.co.uk/thermocouple-information/thermocouple-tolerances.html abgerufen

Thomas Kraft et al. (2024). *Mass flow distribution measurement in concentrated solar power plants via thermal time-of-flight method.*

UNEP. (2023). Von https://www.unep.org/interactives/emissions-gap-report/2023/ abgerufen

UNFCCC. (2016). Von https://unfccc.int/process-and-meetings/the-paris-agreement abgerufen

UNFCCC. (2023). Von https://unfccc.int/news/cop28-agreement-signals-beginning-of-the-end-of-the-fossil-fuel-era abgerufen

Wacker Chemie AG. (2020). *HELISOL Technical Product Brochure*. Von https://www.wacker.com/h/de-de/medias/4_HELISOL_Technical_Product_Brochure.pdf abgerufen

Wacker Chemie AG. (15. 10 2024). *HELISOL XLP Heat Transfer Fluid Extended Technical Data.* Von https://www.wacker.com/h/de-de/medias/20240701_HELISOL_XLP_extended_technical_data.pdf abgerufen

Wang Ruidong and MA. (2021). *Status and Future Development Prospects of CSP.*

WEForum. (2020). Von https://www.weforum.org/agenda/2020/12/renewables-energy-price-cost-cheap-climate-change-sustainability/ abgerufen

Wehner, K. (2022). *Techno-economic evaluation of a full heat transfer fluid change-over in an existing parabolic trough power plant .*

9 Appendix

9.1 Appendix A – Low Boiling Compounds in Helisol HTF (equilibrated at 425°C)

Low Boiling Compounds in HELISOL® HTF (equilibrated @425 °C)

Compound		Elemental formula	Boiling point (1013 hPa)
Hexamethyl -cyclotrisiloxane	D3	C6 H18 O3 Si3	135 °C
Octamethyl -cyclotetrasiloxane	D4	C8 H24 O4 Si4	175 °C
Decamethyl- cyclopentasiloxane	D5	C10 H30 O5 Si5	210 °C
Dodecamethyl- cyclohexasiloxane	D6	C12 H36 O6 Si6	245 °C
Hexamethyl- disiloxane	Si2	C6 H18 O1 Si2	100 °C
Octamethyl- trisiloxane	Si3	C8 H24 O2 Si3	152 °C
Decamethyl- tetrasiloxane	Si4	C10 H30 O3 Si4	194 °C
Dodecamethyl- pentasiloxane	Si5	C12 H36 O4 Si5	230 °C
Tetradecamethyl -hexasiloxan	Si6	C14 H42 O5 Si6	246 °C
Hexadecamethyl -heptasiloxane	Si7	C16 H48 O6 Si7	287 °C
Octadecamethyl -octasiloxane	Si8	C18 H54 O7 Si8	311 °C

WACKER Low Boiling Compounds in HELISOL® HTF
Dr. Kai Schickedanz, 2020 08 18

9.2 Appendix B - Pressure dependent liquid density and heat capacity values of HELISOL XLP in use (Wacker Chemie AG, 2024)

Temperature		Density [kg/m³]				Heat Capacity [kJ/kg·K]			
°C	°F	1 bar	10 bar	20 bar	30 bar	1 bar	10 bar	20 bar	30 bar
-40	-40	1.010,6	1.012,3	1.014,2	1.016,1	1,373	1,374	1,374	1,374
-35	-31	1.004,9	1.006,7	1.008,6	1.010,5	1,379	1,379	1,379	1,379
-30	-22	999,4	1.001,2	1.003,2	1.005,1	1,384	1,385	1,385	1,385
-25	-13	993,9	995,7	997,8	999,7	1,390	1,391	1,391	1,391
-20	-4	988,5	990,4	992,4	994,4	1,397	1,397	1,397	1,397
-15	5	983,2	985,1	987,2	989,2	1,404	1,404	1,404	1,404
-10	14	977,9	979,9	982,0	984,1	1,411	1,411	1,411	1,411
-5	23	972,7	974,7	976,8	979,0	1,419	1,419	1,419	1,419
0	32	967,5	969,5	971,7	973,9	1,427	1,427	1,426	1,426
5	41	962,4	964,5	966,7	968,9	1,435	1,435	1,435	1,435
10	50	957,3	959,4	961,7	964,0	1,443	1,443	1,443	1,443
15	59	952,3	954,4	956,7	959,0	1,452	1,452	1,452	1,452
20	68	947,2	949,4	951,8	954,2	1,461	1,461	1,461	1,460
25	77	942,2	944,5	946,9	949,3	1,471	1,470	1,470	1,470
30	86	937,2	939,5	942,0	944,5	1,480	1,480	1,479	1,479
35	95	932,3	934,6	937,2	939,7	1,490	1,490	1,489	1,489
40	104	927,3	929,7	932,3	934,9	1,500	1,499	1,499	1,498
45	113	922,4	924,8	927,5	930,1	1,510	1,510	1,509	1,508
50	122	917,4	919,9	922,7	925,3	1,520	1,520	1,519	1,518
55	131	912,5	915,1	917,9	920,6	1,531	1,530	1,529	1,529
60	140	907,6	910,2	913,1	915,9	1,541	1,541	1,540	1,539
65	149	902,6	905,3	908,3	911,1	1,552	1,551	1,550	1,550
70	158	897,7	900,5	903,5	906,4	1,563	1,562	1,561	1,560
75	167	892,7	895,6	898,6	901,6	1,574	1,573	1,572	1,571
80	176	887,8	890,7	893,8	896,9	1,585	1,584	1,583	1,582
85	185	882,8	885,8	889,0	892,2	1,596	1,595	1,594	1,593
90	194	877,8	880,9	884,2	887,4	1,608	1,606	1,605	1,604
95	203	872,8	875,9	879,3	882,6	1,619	1,618	1,616	1,615
100	212	867,7	871,0	874,5	877,9	1,630	1,629	1,628	1,626
105	221	862,7	866,0	869,6	873,1	1,642	1,640	1,639	1,637
110	230	857,6	861,0	864,7	868,3	1,654	1,652	1,650	1,649
115	239	852,5	856,0	859,8	863,5	1,665	1,663	1,662	1,660
120	248	847,3	850,9	854,8	858,6	1,677	1,675	1,673	1,671
125	257	842,1	845,9	849,9	853,7	1,689	1,687	1,685	1,683
130	266	836,9	840,7	844,9	848,9	1,701	1,698	1,696	1,694
135	275	831,6	835,6	839,8	843,9	1,712	1,710	1,708	1,706
140	284	826,3	830,4	834,8	839,0	1,724	1,722	1,720	1,717
145	293	820,9	825,2	829,7	834,0	1,736	1,734	1,731	1,729
150	302	815,5	819,9	824,5	829,0	1,748	1,746	1,743	1,740
155	311	810,0	814,6	819,4	824,0	1,760	1,758	1,755	1,752
160	320	804,5	809,2	814,1	818,9	1,773	1,770	1,766	1,764
165	329	798,9	803,8	808,9	813,8	1,785	1,781	1,778	1,775
170	338	793,3	798,3	803,6	808,6	1,797	1,794	1,790	1,787
175	347	787,5	792,7	798,2	803,4	1,809	1,806	1,802	1,799
180	356	781,7	787,1	792,8	798,2	1,822	1,818	1,814	1,810
185	365	775,9	781,5	787,3	792,9	1,834	1,830	1,826	1,822
190	374	769,9	775,7	781,8	787,6	1,847	1,842	1,838	1,834

195	383		769,9	776,3	782,2		1,854	1,849	1,845
200	392		764,1	770,6	776,8		1,867	1,861	1,857
205	401		758,1	764,9	771,3		1,879	1,873	1,869
210	410		752,1	759,1	765,7		1,891	1,885	1,881
215	419		746,0	753,3	760,2		1,904	1,898	1,892
220	428		739,8	747,4	754,5		1,916	1,910	1,904
225	437		733,4	741,4	748,8		1,929	1,922	1,916
230	446		727,0	735,3	743,0		1,942	1,934	1,928
235	455		720,5	729,2	737,2		1,954	1,946	1,939
240	464		713,9	723,0	731,2		1,967	1,958	1,951
245	473		707,2	716,6	725,2		1,980	1,971	1,963
250	482		700,3	710,2	719,2		1,993	1,983	1,975
255	491		693,3	703,7	713,0		2,006	1,995	1,987
260	500		686,1	697,1	706,8		2,020	2,008	1,999
265	509		678,9	690,3	700,5		2,033	2,021	2,011
270	518		671,4	683,5	694,2		2,047	2,033	2,023
275	527		663,8	676,5	687,7		2,061	2,046	2,035
280	536		656,0	669,4	681,1		2,075	2,059	2,046
285	545		648,0	662,2	674,5		2,090	2,072	2,058
290	554		639,8	654,8	667,7		2,105	2,085	2,070
295	563		631,3	647,3	660,9		2,120	2,098	2,082
300	572		622,6	639,7	653,9		2,135	2,111	2,095
305	581		613,7	631,9	646,9		2,151	2,124	2,107
310	590		604,5	623,9	639,7		2,168	2,138	2,119
315	599		594,9	615,7	632,4		2,185	2,151	2,131
320	608		585,0	607,4	625,0		2,203	2,165	2,143
325	617		574,6	598,8	617,5		2,222	2,179	2,155
330	626		563,9	590,0	609,9		2,242	2,194	2,167
335	635		552,6	581,1	602,1		2,264	2,208	2,179
340	644		540,7	571,8	594,2		2,287	2,223	2,191
345	653			562,4	586,2			2,238	2,204
350	662			552,6	578,1			2,253	2,216
355	671			542,6	569,8			2,268	2,228
360	680			532,3	561,4			2,284	2,239
365	689			521,7	552,9			2,300	2,251
370	698			510,8	544,2			2,316	2,263
375	707			499,5	535,4			2,332	2,275
380	716			487,9	526,5			2,348	2,286
385	725			475,9	517,5			2,365	2,297
390	734			463,6	508,4			2,380	2,308
395	743			451,0	499,1			2,396	2,318
400	752			438,0	489,8			2,410	2,328
405	761			424,8	480,5			2,423	2,338
410	770			411,4	471,1			2,435	2,347
415	779			397,9	461,6			2,443	2,355
420	788			384,4	452,2			2,449	2,363
425	797			371,1				2,452	